Geochemistry Geophysics Geosystems G3

Article
Volume 12, Number 9
15 September 2011
Q0AC15, doi:10.1029/2011GC003585
ISSN: 1525-2027

Published by AGU and the Geochemical Society

Multiscale chemical heterogeneities beneath the eastern Southwest Indian Ridge (52°E–68°E): Trace element compositions of along-axis dredged peridotites

Monique Seyler
UFR Sciences de la Terre, CNRS FRE 3298, Géosystèmes, Université Lille 1, Bâtiment SN5, Cité Scientifique, F-59655 Villeneuve d'Ascq CEDEX, France (monique.seyler@univ-lille1.fr)

Daniele Brunelli
Dipartimento di Scienze della Terra, Università di Modena, Largo S. Eufemia 19, I-41100 Modena, Italy (daniele.brunelli@unimore.it)

ISMAR-CNR, via Gobetti 101, I-40129 Bologna, Italy

Géosciences Marines, IPGP-CNRS UMR 715, 1 rue Jussieu, F-75238 Paris CEDEX 05, France

Michael J. Toplis
Institut de Recherche en Astrophysique et Planétologie, CNRS-UMR5277, Université de Toulouse III, 14 Av. Edouard Belin, F-31400 Toulouse, France (toplis@dtp.obs-mip.fr)

Catherine Mével
Institut de Physique du Globe de Paris, Sorbonne Paris Cité, Univ. Paris Diderot, CNRS UMR 7154, F-75005 Paris CEDEX 05, France (mevel@ipgp.jussieu.fr)

[1] The Southwest Indian Ridge is characterized by frequent outcrops of mantle rocks in a very slow spreading context. In situ measurements of trace element concentrations in pyroxenes of these rocks, and associated petrogenetic modeling, are reported. Overall, the measured compositions cover the whole range typically observed for abyssal peridotites. The greatest subkilometer-scale compositional variability is observed in the region east of the Melville fracture zone. The best explanation for the observed variability is given by concurrent melting and migration of melts strongly enriched in the most incompatible rare earth elements, such as those produced by a garnet-bearing source, or by refertilization with mixed garnet- and spinel-derived partially aggregated melts. Because the regionally associated basalts bear no "garnet signature" in their chemical compositions, we conclude that the residual mantle preserves the signature of a mantle source component that does not appear in the erupted magmas. Comparison between along-axis variations of basalt isotopic compositions and peridotite chemical compositions suggests that local isotopic enrichments displayed by some basalts can be associated with the "garnet signature" in the peridotite and that our sampling represents only a fraction of the global variability of the subaxial mantle. To the west of the Melville fracture zone, samples are more depleted and homogeneous at dredge scale. In addition to containing enriched components, petrologic modeling indicates that the peridotitic mantle beneath the entire section underwent (previous?) partial melting in the garnet stability field before melting at lower pressures.

Components: 19,600 words, 12 figures, 4 tables.

Keywords: Indian Ocean; abyssal peridotite; mantle heterogeneities; trace elements; ultraslow spreading ridge.

Index Terms: 1032 Geochemistry: Mid-oceanic ridge processes (3614, 8416); 1037 Geochemistry: Magma genesis and partial melting (3619); 1065 Geochemistry: Major and trace element geochemistry.

Received 28 February 2011; **Revised** 19 May 2011; **Accepted** 3 July 2011; **Published** 15 September 2011.

Seyler, M., D. Brunelli, M. J. Toplis, and C. Mével (2011), Multiscale chemical heterogeneities beneath the eastern Southwest Indian Ridge (52°E–68°E): Trace element compositions of along-axis dredged peridotites, *Geochem. Geophys. Geosyst.*, *12*, Q0AC15, doi:10.1029/2011GC003585.

Theme: Geochemical Heterogeneities in Oceanic Island Basalt and Mid-ocean Ridge Basalt Sources: Implications for Melting Processes and Mantle Dynamics
Guest Editors: C. Beier and P. Asimow

1. Introduction

[2] Abyssal peridotites are the shallowest residues of passive decompressional melting of the upper mantle beneath mid-ocean ridges. As such, these rocks potentially provide valuable information on the workings of ocean ridges and the generation of mid-ocean ridge basalts (MORB). At the scale of a melting domain and along continuous ridge sections of uniform spreading rate, a homogeneous mantle peridotite is expected to undergo a uniform degree of melting. At the top of the melting region the residual mineralogy is in chemical equilibrium with the last melt generated during fractional or critical melting [*Green and Ringwood*, 1967; *Bottinga and Allègre*, 1978; *Ahern and Turcotte*, 1979; *Green et al.*, 1979; *Dick and Fisher*, 1984; *McKenzie and Bickle*, 1988; *Dick*, 1989; *Johnson et al.*, 1990]. Petrological studies show instead that the residual mantle displays small-scale (<1 km) modal and chemical compositional variations resulting from melt extraction, segregation and transport to the surface. In the shallow partially molten mantle and in the near-solidus region of the thermal boundary layer, rock interaction with ascending melts mainly occurs through reactive porous flow alternatively resulting in enhanced local partial melting or dissolution-reprecipitation processes [*Kelemen et al.*, 1992, 1995; *Asimow*, 1999], weak re-enrichment by lower-degree, partially aggregated melts [*Johnson and Dick*, 1992; *Brunelli et al.*, 2006] and interstitial crystallization of incompletely extracted melts [*Seyler et al.*, 2001; *Hellebrand et al.*, 2002a; *Dick*, 1989]. Other processes, such as high-pressure crystal separation, also contribute to modify the residual compositions through late-stage veining [*Dick et al.*, 1984; *Juteau et al.*, 1990; *Hellebrand et al.*, 2002a; *Dantas et al.*, 2007; *Warren et al.*, 2009].

[3] Small-scale chemical heterogeneities (within a sampling site) have not received much attention until recently; available data suggest that they are more numerous in abyssal peridotites sampled at ultraslow spreading ridges or colder regions of the wordwide ridge system [*Johnson and Dick*, 1992; *Hellebrand et al.*, 2002b; *Hellebrand and Snow*, 2003; *Seyler et al.*, 2003, 2004; *Liu et al.*, 2008; *Warren et al.*, 2009; *Brunelli and Seyler*, 2010; *Warren and Shimizu*, 2010] compared to abyssal peridotites sampled at slow [*Ross and Elthon*, 1997; *Brunelli et al.*, 2006; *Seyler et al.*, 2007; *Godard et al.*, 2008], intermediate [*Hellebrand et al.*, 2002a; *Morishita et al.*, 2009] and fast [*Dick and Natland*, 1996] spreading ridges. This is considered as a consequence of the very slow mantle upwelling that results in highly viscous mantle, which enhances diffuse porous flow and melt-rock reactions and favors melt entrapment and crystallization. These features are associated with large outcrops of ultramafic rocks, thick lithosphere and extremely thin oceanic crust, which have been interpreted to reflect unusually cold thermal structure and very low magma supply [*Bonatti et al.*, 2001; *Cannat et al.*, 2003, 2008; *Dick et al.*, 2003; *Jokat et al.*, 2003; *Michael et al.*, 2003]. In the very slow spreading Southwest Indian Ridge (SWIR), reduced melt supply and major element variability of the basalts have been shown to be controlled by melting processes related to the local thermal structure of the lithosphere and the geometry of the ridge axis [*Cannat et al.*, 2008; *Standish et al.*, 2008].

[4] In addition to compositional heterogeneities generated by partial melting and melt extraction processes beneath the present-day ridge, abyssal peridotites sampled at the SWIR are isotopically variable at all length scales down to the grain scale, even in the sections not influenced by hot spot activity [*Snow et al.*, 1994; *Lee*, 1997; *Salters and Dick*, 2002; *Warren et al.*, 2009]. Mantle heterogeneity along the SWIR is also reflected in the basalt compositions that are mixtures of chemically

and isotopically enriched and depleted melts [*Le Roex et al.*, 1992; *Salters and Dick*, 2002; *Meyzen et al.*, 2003, 2005; *Standish et al.*, 2008]. Isotopic compositions of SWIR peridotites not only encompass those of the spatially associated basalts [*Snow et al.*, 1994], but more recently peridotites have been discovered that extend to more depleted compositions than the basalts, suggesting a pyroxenite component in the mantle source [*Salters and Dick*, 2002] or at least refertilization of the asthenospheric mantle [*Meyzen et al.*, 2003, 2005; *Warren et al.*, 2009]. This observation strengthens the idea that normal MORB mantle coexists with more refractory mantle resulting from older depletion events, in agreement with other abyssal peridotite isotopic compositions [*Brandon et al.*, 2000; *Cipriani et al.*, 2004; *Harvey et al.*, 2006; *Liu et al.*, 2008]. Although relatively rare, these examples demonstrate the ability of abyssal peridotites to record isotopically but also chemically enriched melts [*Seyler et al.*, 2004; *Warren et al.*, 2009; *Brunelli and Seyler*, 2010], providing insight into source heterogeneity. This conclusion is supported by recent numerical experiments which show that residual peridotites are powerful markers of diverse source contributions [*Liang*, 2008; *Stracke and Bourdon*, 2009]. In a different setting, *Mazzucchelli et al.* [2009] observed and modeled examples of direct interaction between pyroxenite melts and peridotite in the Balmuccia peridotite massif (northern Italy). They demonstrate the efficiency of melt-peridotite interaction and melt transport to generate melts with E-MORB composition, such as those sampled along ultraslow spreading ridges.

[5] In this paper we investigate local to regional trace element heterogeneities in a suite of abyssal spinel peridotites dredged in the eastern section of the SWIR, to gain some insight into the length scale of the melting heterogeneities and assess the respective effects of melting-induced and source-inherited heterogeneities. This region has the deepest axial valley of the oceanic ridge system and a very thick thermal lithosphere [*Cannat et al.*, 1999]. In such an unusually cold thermal regime small volumes of deep-seated, poorly aggregated partial melts have reasonable chances to be retained in the partially molten mantle [*Rabinowicz and Toplis*, 2009]. Moreover, residual compositions have greater chance to be modified, as the contrast of compositions (e.g., the degree of disequilibrium) between melt and peridotite is greater, enhancing small-scale heterogeneities in the peridotites. We expect this to be the case when alkaline or garnet-equilibrated melt generated by melting of low solidus lithologies interacts with a depleted peridotite equilibrated in the spinel stability field.

2. Geological Context

[6] The SWIR extends from the Bouvet Triple Junction in the SW to the Rodriguez Triple Junction in the NE. With a mean full spreading rate of ~14 mm/yr it is one of the slowest ridges of the global ridge system [*DeMets et al.*, 1990; *Chu and Gordon*, 1999; *Lemaux et al.*, 2002; *Horner-Johnson et al.*, 2005; *Patriat and Segoufin*, 1988]. Ultraslow spreading ridges such as the SWIR constitute a special class of mid-ocean ridges [*Dick et al.*, 2003], characterized by strong segmentation involving transform faults and non-transform discontinuities, long spreading segments oblique to the direction of ocean floor spreading and shorter near-orthogonal magmatic spreading segments. The thickness of the basaltic crust is highly variable from one segment to another and within individual segments, leaving large exposures of mantle-derived peridotites along the oblique, amagmatic or nearly amagmatic axial regions [*Cannat et al.*, 1999; *Dick et al.*, 2003]. The eastern SWIR (52°E–69°E) is substantially deeper than the central and western SWIR [*Cannat et al.*, 1999; *Sauter et al.*, 2001; *Baines et al.*, 2007; *Cannat et al.*, 2008], and basalt geochemistry suggests significantly lower mantle temperatures and thinner magmatic crust [*Muller et al.*, 1997; *Cannat et al.*, 1999; *Meyzen et al.*, 2003].

[7] The area between 52°E and 68°E was closely sampled along axis by dredging during the EDUL cruise [*Mével et al.*, 1997]. Out of 69 dredges, 13 delivered mantle-derived lherzolites and harzburgites which provided the peridotite sample set of this study (Figure 1). Based on mean axial depth, the style of segmentation and ridge obliquity, this section of the SWIR has been subdivided into two major regions separated by the Melville fracture zone at ~61°E. Between the Gallieni and Melville fracture zones (52°E–61°E), the mean axial depth is ~4330 m [*Cannat et al.*, 1999] and basalt geochemistry and seismic data suggest a crustal thickness of ~4 km [*Muller et al.*, 1997]. The ridge is slightly oblique spreading, but the obliquity is partially accommodated by transform faults with modest offsets (<50 km) and second-order bathymetric segmentation that has persisted through time since the onset of SWIR spreading [*Phipps Morgan and Parmentier*, 1995; *Patriat et al.*, 1997; *Sandwell and Smith*, 1997; *Baines et al.*,

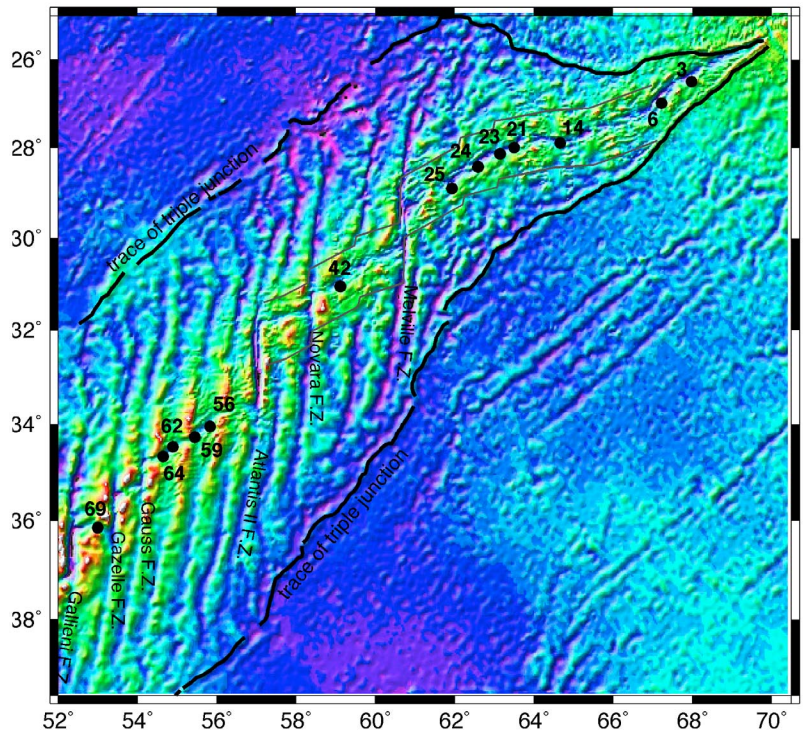

Figure 1. Bathymetric map of the eastern portion of the Southwest Indian Ridge, showing the location of peridotite-bearing dredges from the EDUL cruise. Bathymetry is derived from multichannel shipboard data near the SWIR axis [*Mendel et al.*, 1997] and for off-axis areas [*Smith and Sandwell*, 1994]. Thick lines show the trace of the Rodrigues Triple Junction [*Patriat et al.*, 1997] that separates SWIR crust from Central Indian Ridge and Southeast Indian Ridge crust.

2007]. EDUL Dr69 is located at ~53°E between the Gallieni and Gauss fracture zones. The dredge recovered serpentinized harzburgites along with minor dunites, pyroxenites and gabbros and a few old basalts. These rocks form a small massif in the axial rift valley, which is the deepest of the western region (~4500 m). The region between the Gauss and Atlantis II fracture zones comprises two short, near-amagmatic, oblique spreading segments [*Baines et al.*, 2007]. Dredges Dr62 and Dr64 at ~54°E–55°E and dredges Dr56 and Dr59 at 55°E–56°E yield serpentinized peridotites and gabbros with minor basalts; a few plagioclase-bearing peridotites occur in dredge Dr62. In contrast, between the Atlantis II and Melville fracture zones, a single dredge (dredge Dr42 at ~59°7′E) has recovered serpentinized peridotites with basalt as the dominant lithology. Between the Gauss and Melville fracture zones bathymetric segmentation correlates with gravimetric segmentation defined by the Mantle Bouger Anomaly (MBA) [*Cannat et al.*, 1999; *Rommevaux-Jestin et al.*, 1997]. There is also a very good correlation between increasing regional axial depth and increasing $Na_{8.0}$ in basaltic glasses, which overlaps the global $Na_{8.0}$-depth MORB array of *Klein and Langmuir* [1987] and *Langmuir et al.* [1992], suggesting decreasing degree of melting toward the Melville fracture zone.

[8] Between the Melville fracture zone and the Rodriguez Triple Junction (61°E–70°E), the SWIR axis is devoid of transform zones. This section is characterized by a very deep axial valley (mean axial depth ~4730 m) and strong variability in axial depths and morphology. Based on basalt geochemistry, the mean crustal thickness (~2.7 km) is thinner than for the region west of the Melville fracture zone [*Cannat et al.*, 1999], but seismic data suggest highly variable crustal thickness (2–6 km) at segment scales with an average of ~4 km [*Muller et al.*, 1999]. Two changes in ridge trend at 63°67′E and 66°13′E separate a region with nearly orthogonal spreading (ESR of about 7 mm/yr) from two adjacent regions that have the deepest axial valley of the SWIR (~4740 and 4800 m [*Cannat et al.*, 2008]) and oblique spreading (ESR of about 6 mm/yr). In

each region, along-axis, long melt-poor or avolcanic ridge sections separate prominent volcanic centers. Gravity-derived crustal thickness [*Cannat et al.*, 2006], tied to seismic data [*Minshull et al.*, 2006; *Muller et al.*, 1999], reveal large expanses of seafloor characterized by a smooth and rounded topography, called "smooth seafloor," separated by smaller areas characterized by bathymetric highs and negative MBAs, interpreted as large volcanic centers [*Cannat et al.*, 2003, 2006]. Between the Melville fracture zone and 63°67′E, smooth seafloor constitutes about 50% of the mapped area and provides the main set of serpentinized mantle-derived peridotites dredged along axis (EDUL dredges Dr14, Dr21, Dr23, Dr24, Dr25). The collected samples are dominated by spinel peridotites but plagioclase-bearing peridotites represent ~30% of the mantle derived samples in dredges Dr21 and Dr23 and the near totality of those of Dr14. Minor dunites, gabbros and basalts were also recovered. Between 63°67′ and 66°13′E, smooth seafloor forms about 28% of mapped area, from which no peridotite samples have been recovered. Although very deep, the region east of 66°13′E provided very few peridotites in two dredges. Dredge Dr3 (67°59′E) recovered a single large piece of harzburgite with no gabbro and abundant basalts, while dredge Dr6 (~67°13′E) recovered six hand-sized pieces of lherzolite and five pieces of dunite, some of them being strongly mylonitized.

[9] Basaltic glasses collected in the region east of the Melville fracture zone have unusual compositions [*Meyzen et al.*, 2003]. They are highly enriched in Na_2O but do not plot on the $Na_{8.0}$-$Fe_{8.0}$ and $Na_{8.0}$-regional axial depth global MORB trends of *Klein and Langmuir* [1987] and *Langmuir et al.* [1992] and show poor correlation with gravimetry [*Cannat et al.*, 1999]. These features suggest higher mean pressure of mantle melting and lower mantle temperature and/or more depleted mantle east of the Melville fracture zone. Major element compositions of the mantle-derived peridotites [*Seyler et al.*, 2003, 2004] also show large heterogeneities of the axial lithospheric mantle at regional and local scales, east and west of the Melville fracture zone, and these heterogeneities are stronger in the easternmost region. Both the basalt and peridotite compositions suggest strong chemical interaction between upwelling upper mantle and percolating melts in a context of thick axial lithosphere and low melt productivity, particularly prevalent east of the Melville fracture zone [*Meyzen et al.*, 2003; *Seyler et al.*, 2003, 2004]. This is possibly related to a heterogeneous MORB mantle source, as shown by the isotopic compositions of basalts [*Meyzen et al.*, 2005].

3. Sample Selection and Characteristics

[10] Twenty-four samples were selected from the thirteen EDUL dredges which collected peridotites. They are moderately altered spinel perodotites, with 60–75% serpentinization, which preserved primary coarse granular textures showing little plastic deformation and dynamic recrystallization. Dredge Dr6 peridotites are exceptions in that they display porphyroclastic textures defined by centimeter-sized Opx and Cpx porphyroclats in a recrystallized olivine matrix. All samples are devoid of magmatic veins, lack plagioclase or its alteration products and contain low-Ti spinels ($TiO_2 < 0.2\%$). Major element compositions of the primary minerals are generally restricted in range from sample to sample in individual dredges, even in those characterized by large modal variations. Based on these features, *Seyler et al.* [2003] concluded that the samples are texturally mantle residues fully equilibrated in the spinel peridotite field. For detailed microstructure study, modal data and major element compositions of the primary mineral phases the reader is referred to *Seyler et al.* [2003]. Additional modal analyses (Table 1) and determinations of major element compositions of the Cpx and Opx are reported in Tables S1 and S2 in the auxiliary material.[1]

[11] Five dredges brought up large amounts (300–1000 kg) of peridotites, allowing us to study the chemical variability at a subkilometer scale and possible correlations between major and trace element compositions. Among them, dredges Dr21 and Dr23 east of the Melville fracture zone contain spinel peridotites characterized by huge variations in modal composition from sample to sample; they range from lherzolites (5–10% modal Cpx) to olivine-rich harzburgites (2- < 5% modal Cpx) and virtually Cpx-free, olivine-poor harzburgites [*Seyler et al.*, 2003, 2004]. We selected four samples from dredge Dr21 (Dr21-5-1, Dr21-5-2, Dr21-5-3, Dr21-7-2) and three samples from dredge Dr23 (Dr23-2-5, Dr23-2-8, Dr23-3-2) as representative of the whole modal range. In contrast, spinel peridotites from dredges Dr56, Dr62 and Dr64 west of the Melville fracture zone display homogeneous modal distributions falling at the lherzolite-harzburgite boundary (5 ± 1% modal

[1] Auxiliary materials are available in the HTML. doi:10.1029/2011GC003585.

Table 1. Reconstructed Primary Modal Compositions of the EDUL Peridotites of This Study[a]

	Primary Phase Minerals (vol. %)			
	Olivine	Orthopyroxene	Clinopyroxene	Spinel
EDUL Dr3-1	71.4	24.1	3.8	0.6
EDUL Dr6-1-2[b]	67.2	22.6	9.7	0.5
EDUL Dr6-1-3	67.7	24.3	7.6	0.4
EDUL Dr21-5-1	68.2	25.9	4.9	1.0
EDUL Dr21-5-2	66.0	25.2	8.4	0.4
EDUL Dr21-5-3	68.7	22.7	7.3	1.3
EDUL Dr21-7-2[b]	70.7	26.9	2.1	0.3
EDUL Dr23-2-5	68.4	21.3	8.5	1.8
EDUL Dr23-2-8	68.5	21.6	9.0	0.9
EDUL Dr23-3-2	70.3	22.6	5.9	1.2
EDUL Dr24-1[b]	69.6	23.4	5.8	1.2
EDUL Dr25-3-1	75.2	20.4	4.1	0.4
EDUL Dr42-4-3	65.7	30.6	2.7	1.0
EDUL Dr56-3-5	67.0	25.6	6.4	1.0
EDUL Dr56-3-8	69.8	24.8	4.5	1.0
EDUL Dr56-3-11	69.8	23.9	5.3	1.0
EDUL Dr59-2-2	73.6	22.2	3.5	0.7
EDUL Dr62-4-2	69.8	25.3	4.2	0.7
EDUL Dr64-1-5	67.3	27.4	4.1	1.2
EDUL Dr69-1-1[c]	59.3	35.6	2.2	2.9
EDUL Dr69-1-10	64.4	31.6	3.1	1.0
EDUL Dr69-8-2	19.8	2.1	76.4	4.7

[a]The modes were determined by technics described by *Seyler et al.* [2003].
[b]Small-sized sample; mode may not be representative.
[c]Sample contains two populations of Cpx (see text for explanation).

Cpx). Three samples from dredge Dr56 (Dr56-3-5, Dr56-3-8, Dr56-3-11) and two other samples (Dr62-4-2 and Dr64-1-5) were selected to represent compositionally homogeneous dredges. Dredges Dr25 and Dr59 also contained large amounts of peridotite but samples are highly altered with most pyroxenes replaced by low-temperature amphibole and/or too strongly serpentinized to recognize the primary textures. These two dredges are thus represented by only one sample each, Dr25-3-1 and Dr59-2-1 which are free of amphibole and among the least serpentinized.

[12] In spite of the paucity of available material, *Seyler et al.* [2003] have distinguished two groups among Dr6 lherzolites, one containing Cr-poor pyroxenes and Cr-poor spinels, the other containing Cr-rich pyroxenes and Cr-rich (low-Ti) spinels. The three selected samples are representative of this bimodality. Dr6-1-3 represents the low-Cr group and Dr6-1-1 and Dr6-1-2 represent the high-Cr group. Samples Dr3-1, Dr14-1, Dr24-1 and Dr42-4-3 are from the other dredges which collected very few ultramafics.

[13] Dredge Dr69 harburgites differ from typical abyssal peridotites. They are olivine-poor, Opx-rich harzburgites (27–35% modal Opx), containing ~2% of small-sized (<0.5 mm), interstitial Cpx. Their mineral chemistry reflect unusually high whole rock Cr/Al and Mg/Fe, indicative of strong depletion by melt extraction [*Seyler et al.*, 2003]. Sample Dr69-1-10 is a representative sample while sample Dr69-1-1 contains patches of Cpx a few mm in size scattered in the serpentinized matrix. These coarse Cpx do not differ from the interstitial Cpx grains in terms of major element composition. A clinopyroxenite sample (Dr69-8-2) has been included in this study. It consists of a hand-sized fragment containing millimeter-sized Cpx grains, with subordinate amounts of Opx, olivine and spinel. Its spatial relationships with the surrounding harzburgite are unknown, but a cumulate origin related to the gabbroic intrusions is suggested by the mineralogic continuity from spinel pyroxenite through plagioclase-bearing pyroxenite to olivine gabbro, and by major element compositions of their Cpx that are distinct from those of the residual peridotites.

4. Methods

[14] In situ trace element analyses were measured by secondary ion microprobe spectrometry (SIMS) with the Cameca IMS5f at the university of Montpellier 2. ^{47}Ti, ^{88}Sr, ^{89}Y, ^{90}Zr, ^{137}Ba, ^{139}La, ^{140}Ce,

^{143}Nd, ^{147}Sm, ^{151}Eu, ^{160}Gd, ^{163}Dy, ^{167}Er and ^{174}Yb were measured in all sessions; ^{141}Pr, ^{159}Tb and ^{175}Lu were measured in some sessions. Each spot was measured using 10 cycles with counting times of 2 s for Ti, Sr, Y and Zr and of 40 s for Ba and the rare earths. Concentrations were calibrated against the SRM NIST 610 glass using the values given by *Rocholl et al.* [1997]. Repeated analyses show a precision of 5% (1 sigma). ^{30}Si were used as an internal standard to correct for differences between standard and samples, based on the EMP analyses. The effects of most molecular interferences are eliminated in following the energy filtering technique described by *Shimizu et al.* [1978]. More specifically, due to the low concentrations measured in pyroxenes of abyssal peridotites, eight REE oxides produce significant interferences $^{135}BaO^+$ with $^{151}Eu^+$, $^{143}NdO^+$ with $^{159}Tb^+$, $^{144}NdO^+$ and $^{144}SmO^+$ with $^{160}Gd^+$, $^{147}SmO^+$ with $^{163}Dy^+$, $^{151}EuO^+$ with Er+, $^{160}GdO^+$ with $^{174}Yb^+$, $^{159}TbO^+$ with $^{175}Lu^+$. The MO^+/M^+ ratios used for the corrections are 0.0047, 0.14, 0.27, 0.02, 0.08, 0.07, 0.33 and 0.28, respectively (with errors <10%). Corrections are <2% of the measured element/Si ratios for Eu, Gd, Dy and Er, and <5% for Yb. These corrections and treatment of other analytical results follow the procedures described by *Zinner and Crozaz* [1986], *Bottazzi et al.* [1992], *Fahey* [1998] and *Plá Cid et al.* [2005]. Overall precision taking into account all the sources of uncertainty is estimated to be 10% for each oxide/element ratio.

[15] A subset of pyroxenes was also analyzed on polished thick sections by inductively coupled plasma–mass spectrometry (ICP-MS) coupled with laser ablation (LA) at the university of Montpellier 2. The LA system is an automated platform Microlas (Geolas Q+) equipped with a 193 nm laser Excimer CompEx 102 from LambdaPhysik. Data were obtained in three sessions. The first series of measurements (samples Dr23-2-5 and Dr23-2-8) was performed using a 1991 vintage VG Plasmaquad II turbo ICP-MS with a sensitivity of ca.100 million cps/ppm measured on ^{115}In. The other two series were analyzed on a ThermoFinnigan Element 2 High Resolution ICP-MS (HR-ICP-MS) using a single collector double-focusing field Element XR (eXtended Range) with an improved sensitivity of ca. 1 billion cps/ppm on ^{115}In. Analyses were performed using an in-house modified ablation cell of 30 cm^3 in a helium atmosphere [*Günther and Heinrich*, 1999]. A laser energy density of 15 Jcm^{-2} was used at a frequency of 5 Hz and spot sizes of 120 μm for Opx and 100 μm for Cpx. Signals were acquired in Time Resolved Acquisition mode, for 120 s for the blank and 60 s for measurement. The resulting sensitivity is approximately 4000 cps/ppm on ^{115}In. Concentrations were calibrated against the SRM NIST 612 rhyolitic glass using the values given by *Pearce et al.* [1997]. ^{29}Si was used as the internal standard and ^{43}Ca was also measured. Data were reduced using the GLITTER software [*Van Achterberg et al.*, 2001]. Precision of the analyses, assessed by repeated analyses of reference NIST SRM 612 and basalt BR, varies from 5 to 10%. Average compositions of the standards and 1 sigma error are given in Table S3.

[16] Consistency between SIMS and LA-ICP-MS measurements was checked by analyzing several samples with both techniques. Elemental concentrations >2 ppm tend to deviate slightly from the 1:1 line, as standard deviations increase (Figure S1); in general, SIMS concentrations are slightly more scattered. Although the clearest and freshest domains of pyroxene grains were selected, submicron sized cracks and alteration veinlets following the crystallographic directions could not be avoided. In agreement with *Dijkstra et al.* [2010], anomalously high counts of Pb, U, Ba, and to a lesser extent Sr, are attributed to microheterogeneities. Opx is particularly sensitive to alteration effects due to its extremely low trace element content and to the fact that it is more alterable than Cpx. Nevertheless, LA-ICP-MS and ion probe concentrations are within analytical errors for the REEs and differences are not significant in individual samples for all the elements which have been tested. Therefore, LA-ICP-MS and SIMS measurements for each sample have been averaged when their differences are within analytical errors (Tables 2 and 3). Complete trace element data of Opx and Cpx obtained with the two techniques are available in the auxiliary material (Tables S4–S7).

5. Analytical Results

5.1. Trace Element Compositions of Clinopyroxenes

[17] Rare earth element (REE) and other significant incompatible trace element (Sr, Zr, Ti, Y) concentrations have been normalized to C1 chondrite of *Anders and Grevesse* [1989] and plotted in Figure 2. East of the Melville fracture zone, Cpx grains are unzoned and show no significant differences in trace element contents from grain to

Table 2. Trace Element Concentrations in ppm for Clinopyroxenes of EDUL Peridotite Samples Analyzed in This Study[a]

Sample	N	Ti	SD	Sr	SD	Y	SD	Zr	SD	Ba	SD	La	SD	Ce	SD	Pr	SD	Nd	SD	Sm
EDUL Dr3-1	5	679	38	4.8	0.5	7.3	0.9	1.14	0.14	0.5081	0.1990	0.0598	0.0021	0.213	0.027	0.042	0.001	0.271	0.029	0.203
EDUL Dr6-1-1	3	822	77	27.4	2.9	6.6	0.4	9.50	1.00	0.3926	0.0698	0.1488	0.0190	0.790	0.107			1.507	0.058	0.684
EDUL Dr6-1-2	14	973	213	30.6	3.5	5.3	0.6	12.21	1.52	3.4876	8.4453	0.6100	0.1176	3.591	0.323	0.731	0.065	3.981	0.419	0.969
EDUL Dr6-1-3	7	1607	115	11.6	1.7	10.5	1.1	6.08	0.50	0.2169	0.1911	0.1064	0.0236	0.596	0.062	0.162	0.014	1.244	0.075	0.715
EDUL Dr14-2-1	7	1384	125	7.9	1.1	11.0	0.4	3.10	0.34	0.0633	0.0453	0.0858	0.0047	0.337	0.030	0.096	0.008	0.727	0.039	0.555
EDUL Dr21-5-1	4	1467	111	2.9	0.6	12.2	0.2	3.74	0.44	0.1619	0.0907	0.0283	0.0097	0.173	0.032	0.077	0.010	0.859	0.040	0.752
EDUL Dr21-5-2	2	2335	338	2.1	0.3	15.6	0.9	5.20	0.54	0.0927	0.0026	0.0220	0.0129	0.268	0.006	0.136	0.005	1.297	0.007	0.920
EDUL Dr21-5-3	2	1753	370	3.1	0.3	14.8	1.7	5.11	1.02	0.0519	0.0308	0.0503	0.0030	0.394	0.015			1.379	0.069	0.900
EDUL Dr21-7-2	5	1966	303	2.0	0.3	14.4	1.1	2.90	0.24	0.0743	0.0392	0.0108	0.0032	0.116	0.006	0.066	0.005	0.744	0.046	0.736
EDUL Dr23-2-5	4	2194	36	12.1	1.2	14.0	1.5	7.92	0.35	0.0293	0.0022	0.1299	0.0066	0.781	0.022	0.207	0.005	1.553	0.047	0.828
EDUL Dr23-2-8	10	1994	156	15.6	2.7	13.7	1.0	10.29	1.23	0.0457	0.0482	0.2118	0.0288	1.055	0.090	0.237	0.009	1.788	0.138	0.907
EDUL Dr23-3-2	3	1414	98	3.5	0.3	13.2	1.6	4.72	0.30	0.0068	0.0022	0.0246	0.0063	0.228	0.020			0.926	0.065	0.693
EDUL Dr23-3-2[b]	1	1382		5.1		13.4		5.15		0.0560		0.0320		0.283				0.992		0.716
EDUL Dr24-1	3	2333	157	8.0	1.1	18.3	0.5	9.68	1.31	0.0140	0.0020	0.0279	0.0025	0.535	0.012	0.253	0.004	2.643	0.290	1.326
EDUL Dr25-3-1	9	730	44	2.4	0.3	7.4	0.7	0.75	0.19	0.0814	0.0546	0.0254	0.0044	0.144	0.014	0.029	0.005	0.255	0.026	0.162
EDUL Dr42-4-3	3	1810	84	0.2	0.1	14.1	0.7	2.46	0.51	1.2702	0.1301	0.0409	0.0271	0.104	0.023	0.021	0.001	0.254	0.008	0.293
EDUL Dr56-3-5	5	922	204	0.6	0.5	9.0	0.7	2.19		0.0467	0.0515	0.0003	[c]	0.005	0.001	0.006	0.001	0.116	0.033	0.217
EDUL Dr56-3-8	5	669	16	1.0	0.2	8.2	0.4	0.23	0.04	0.4803	0.3895	0.0126	0.0114	0.020	0.013	0.006	0.002	0.102	0.023	0.221
EDUL Dr56-3-8[d]	1	697		4.7		9.3		1.72		0.3503		0.2496		0.484				0.474		0.258
EDUL Dr56-3-11	7	823	45	1.2	0.6	7.8	0.7	0.24	0.18	0.0784	0.0246	0.0010	0.0003	0.015	0.006	0.006	0.003	0.122	0.048	0.187
EDUL Dr59-2-2	2	905	189	3.8	0.3	7.6	0.1	0.20	0.07	1.0200	0.1115	0.0228	0.0146	0.021	0.018			0.061	0.006	0.160
EDUL Dr62-4-2	6	483	43	1.8	1.0	6.6	0.7	0.16	0.03	0.1699	0.0942	0.0324	0.0166	0.025	0.015			0.068	0.034	0.102
EDUL Dr62-4-2[e]	1	703		4.5		7.0		0.94		1.1128		0.1451		0.165		0.029		0.337		0.264
EDUL Dr64-1-5	6	378	145	2.0	0.4	5.1	0.2	0.12	0.02	0.0400	0.0171	0.0164	0.0029	0.024	0.017			0.061	0.016	0.038
EDUL Dr64-1-5[d]	1	375		0.4		5.2		0.11		0.0419		0.1704		0.294				0.142		0.060
EDUL Dr69-1-1	11	470	17	0.8	0.7	4.1	0.2	0.21	0.01	0.3176	0.6654	0.0071	0.0097	0.006	0.001			0.025	0.007	0.056
EDUL Dr69-1-1[b]	1	460		2.4		4.4		0.19		0.1945		0.0430		0.025				0.012		0.027
EDUL Dr69-1-1[f]	3	375	43	1.7	0.5	4.0	0.2	0.37	0.09	0.3481	0.0452	0.3374	0.0184	0.568	0.136	0.068	0.014	0.336	0.072	0.124
EDUL Dr69-1-10	4	537	59	4.9	1.5	6.8	0.4	0.65	0.11	0.1171	0.0156	0.0329	0.0282	0.065	0.026	0.013	0.003	0.126	0.024	0.153
EDUL Dr69-8-2	6	491	16	2.1	0.1	5.6	0.3	0.32	0.03	0.1907	0.0675	0.0758	0.0237	0.209	0.046			0.320	0.031	0.225

[a]Compositions average several pyroxene textural types when variations are within analytical errors. N, number of analyses; SD, standard deviation; bdl, below detection limit. Empty values mean not measured.
[b]Exsolution lamellae in orthopyroxene.
[c]Only one measure.
[d]Rim that differs in composition from other grain rims.
[e]Microvein.
[f]Blebs replacing orthopyroxene.

Table 2. (continued)

Sample	SD	Eu	SD	Gd	SD	Tb	SD	Dy	SD	Ho	SD	Er	SD	Tm	SD	Yb	SD	Lu	SD
EDUL Dr3-1	0.013	0.101	0.009	0.578	0.057	0.133	0.015	1.125	0.065	0.2713	0.0244	0.815	0.068	0.1315	0.0011	0.834	0.070	0.1256	0.0090
EDUL Dr6-1-1	0.049	0.336	0.007	1.041	0.024	0.174	0.013	1.183	0.093			0.714	0.071			0.702	0.062	0.1035	0.0049
EDUL Dr6-1-2	0.107	0.331	0.038	0.978	0.111	0.151	0.012	1.007	0.075	0.2047	0.0132	0.564	0.052	0.1	0.0056	0.512	0.042	0.0751	0.0072
EDUL Dr6-1-3	0.040	0.305	0.020	1.280	0.065	0.247	0.017	1.900	0.052	0.4127	0.0177	1.201	0.036	0.1712	0.0068	1.138	0.056	0.1617	0.0033
EDUL Dr14-2-1	0.020	0.269	0.015	1.185	0.018	0.262		1.802	0.066			1.214	0.036			1.158	0.034	0.1675	0.0080
EDUL Dr21-5-1	0.027	0.356	0.021	1.483	0.017	0.287		2.086	0.065			1.299	0.053			1.176	0.038	0.1697	0.0086
EDUL Dr21-5-2	0.040	0.423	0.017	1.912	0.092	0.380	0.023	2.785	0.056	0.6200	0.0311	1.800	0.102	0.2631	0.0233	1.812	0.204	0.2386	0.0113
EDUL Dr21-5-3	0.023	0.382	0.033	1.678	0.144	0.331	0.046	2.444	0.352			1.538	0.201			1.400	0.178	0.1904	0.0218
EDUL Dr21-7-2	0.072	0.317	0.015	1.527	0.097	0.322	0.045	2.315	0.157	0.5501	0.1130	1.564	0.121	0.2248	0.0124	1.498	0.144	0.2070	0.0247
EDUL Dr23-2-5	0.030	0.345	0.018	1.535	0.060	0.303	0.005	2.239	0.079	0.5187	0.0232	1.447	0.079	0.2176	0.0037	1.352	0.090	0.1906	0.0199
EDUL Dr23-2-8	0.089	0.378	0.035	1.583	0.127	0.294	0.012	2.252	0.123	0.4860	0.0179	1.452	0.103	0.1998	0.0095	1.324	0.070	0.1926	0.0182
EDUL Dr23-3-2	0.075	0.317	0.041	1.420	0.143	0.281	0.042	2.029	0.178			1.355	0.173			1.240	0.151	0.1732	0.0218
EDUL Dr23-3-2[b]		0.328		1.457		0.281		2.028				1.353				1.188		0.1617	
EDUL Dr24-1	0.013	0.588	0.014	2.212	0.093	0.425	[c]	2.975	0.129			1.773	0.063			1.563	0.103	0.2181	0.0145
EDUL Dr25-3-1	0.013	0.085	0.006	0.495	0.035	0.121	0.010	1.106	0.090	0.2718	0.0266	0.875	0.076	0.1331	0.0140	0.912	0.119	0.1338	0.0147
EDUL Dr42-4-3	0.018	0.164	0.014	0.976	0.010	0.250	[c]	2.127	0.102			1.544	0.125			1.419	0.010	0.2064	0.0174
EDUL Dr56-3-5	0.039	0.120	0.008	0.692	0.023	0.160	0.000	1.489	0.085	0.3458	0.0223	1.065	0.066	0.1534	0.0089	1.087	0.047	0.1589	0.0024
EDUL Dr56-3-8	0.034	0.122	0.013	0.763	0.049	0.152	[c]	1.255	0.042			0.949	0.006			0.903	0.048	0.1412	0.0073
EDUL Dr56-3-8[d]		0.117		0.755				1.464				0.966				0.993		0.1369	
EDUL Dr56-3-11	0.014	0.104	0.017	0.614	0.067	0.152	0.018	1.266	0.112	0.3056	0.0223	0.905	0.071	0.1424	0.0132	0.936	0.099	0.1375	0.0131
EDUL Dr59-2-2	0.012	0.084	0.001	0.496	0.062	0.130	[c]	1.094	0.014			0.941	0.011			0.898	0.029	0.1397	0.0072
EDUL Dr62-4-2	0.015	0.062	0.012	0.396	0.037	0.109	0.007	0.959	0.096			0.789	0.066			0.797	0.089	0.1256	0.0090
EDUL Dr62-4-2[e]		0.110		0.534				0.970				0.799				0.805		0.1132	
EDUL Dr64-1-5	0.003	0.028	0.003	0.265	0.027			0.656	0.039			0.598	0.025			0.641	0.059	0.0955	0.0097
EDUL Dr64-1-5[d]		0.031		0.289		0.079		0.663				0.599				0.640		0.0930	
EDUL Dr69-1-1	0.009	0.024	0.004	0.228	0.012	0.062	0.003	0.567	0.028			0.472	0.027			0.487	0.029	0.0678	0.0068
EDUL Dr69-1-1[b]		0.021		0.194				0.555				0.484				0.449		0.0548	
EDUL Dr69-1-1[f]	0.004	b,d,l,		0.265	0.046			0.557	0.011			0.464	0.014			0.460	0.036		
EDUL Dr69-1-10	0.005	0.075	0.011	0.595	0.085	0.119	[c]	1.106	0.094			0.787	0.040			0.795	0.054	0.0892	0.0139
EDUL Dr69-8-2	0.019	0.091	0.013	0.459	0.032	0.101	0.007	0.789	0.091			0.566	0.061			0.559	0.043	0.0769	0.0058

Table 3. Trace Element Concentrations in ppm for Orthopyroxenes of EDUL Peridotite Samples Analyzed in This Study[a]

	N	Ti	SD	Sr	SD	Y	SD	Zr	SD	Ba	SD	La	SD	Ce	SD	Pr	SD	Nd	SD	Sm
EDUL Dr3-1	6	309	5	0.54	0.46	1.01	0.06	0.31	0.31	0.222	0.246	0.0086	0.0064	0.0151	0.0123	0.0022	0.0019	0.0178	0.0015	0.0144
EDUL Dr6-1-1	6	352	70	1.26	0.42	0.73	0.04	1.27	0.16	0.064	0.060	0.0089	0.0064	0.0293	0.0082	0.0084	0.0020	0.0543	0.0055	0.0321
EDUL Dr6-1-2	2	425	19	0.49	0.17	0.62	0.03	1.38	0.11	0.023	0.029	0.0072	0.0015	0.0390	0.0074	0.0095	0.0008	0.0634	0.0121	0.0266
EDUL Dr6-1-3	3	682	56	0.58	0.48	1.34	0.23	1.10	0.12	0.571	0.122	0.0017	0.0004	0.0135	0.0033	0.0052	0.0018	0.0342	0.0082	0.0281
EDUL Dr21-5-2	2	808	43	0.62	0.12	1.94	0.15	0.62	0.25	0.057	0.051	bdl		0.0086	[b]	0.0026	[b]	0.0322	0.0034	0.0318
EDUL Dr 21-7-2	3	813	49	0.11	0.03	1.61	0.16	0.44	0.06	0.069	0.092	0.0008	0.0001	0.0042	0.0012	0.0010	0.0007	0.0158	0.0047	0.0243
EDUL Dr23-2-5	2			0.17	0.00	1.82	0.13	1.34	0.15	0.031	[b]	bdl		0.0134	0.0011	bdl		0.0376	0.0009	0.0325
EDUL Dr23-2-8	5	915	79	0.35	0.10	1.40	0.04	1.23	0.05	0.017	0.008	0.0050	0.0028	0.0243	0.0169	0.0063	0.0035	0.0355	0.0133	0.0287
EDUL Dr25-3-1	3	240		0.30	[c]	0.89	0.11	0.11	0.00	0.030	[c]	bdl		bdl		bdl		bdl		bdl
EDUL Dr23-3-2[d]	1	370		0.06		0.85		0.43		0.010		0.0014		0.0021				0.0047		0.0086
EDUL Dr23-3-2	1	442		0.37		1.63		0.82		0.009		0.0037		0.0201				0.0713		0.0547
EDUL Dr56-3-5	2	302	48	3.43	0.13	0.92	0.26	0.01	0.01	0.122	0.014	0.0028	0.0002	0.0020	0.0006	0.0006	[b]	0.0063	[b]	0.0057
EDUL Dr56-3-11	4	363	29	0.12	0.10	1.34	0.18	2.23	4.36	0.026	0.013	0.0315	0.0440	0.0566	0.0609	bdl		0.0099	0.0075	0.0100
EDUL Dr69-1-1[e]	1	198		bdl		0.65						0.0202		0.0146		0.0078		0.0448		0.0930
EDUL Dr69-1-1	2	251	158	0.07	0.01	0.52	0.03	1.25	[c]	0.006	0.002	0.0007	0.0008	0.0020	0.0008			0.0049	0.0019	0.0023

	SD	Eu	SD	Gd	SD	Tb	SD	Dy	SD	Ho	SD	Er	SD	Tm	SD	Yb	SD	Lu	SD
EDUL Dr3-1	0.0086	0.0100	0.0047	0.0365	0.0205	0.0124	0.0058	0.126	0.021	0.0382	0.0038	0.146	0.013	0.0277	0.0031	0.217	0.024	0.0411	0.0045
EDUL Dr6-1-1	0.0060	0.0161	0.0031	0.0591	0.0080	0.0121	0.0013	0.110	0.013	0.0294	0.0027	0.098	0.008	0.0185	0.0020	0.159	0.010	0.0277	0.0023
EDUL Dr6-1-2	0.0073	0.0129	0.0037	0.0451	0.0020	0.0096	0.0020	0.097	0.016	0.0227	0.0000	0.087	0.003	0.0188	0.0030	0.131	0.003	0.0259	0.0023
EDUL Dr6-1-3	0.0087	0.0159	0.0029	0.0763	0.0215	0.0172	0.0046	0.180	0.046	0.0522	0.0091	0.186	0.032	0.0361	0.0071	0.305	0.029	0.0558	0.0039
EDUL Dr21-5-2	0.0111	0.0209	0.0080	0.1094	0.0301	0.0265	0.0053	0.274	0.051	0.0724	0.0138	0.261	0.021	0.0494	0.0035	0.394	0.009	0.0654	0.0100
EDUL Dr 21-7-2	0.0071	0.0132	0.0059	0.0832	0.0281	0.0222	0.0065	0.186	0.024	0.0604	0.0070	0.205	0.024	0.0372	0.0078	0.300	0.071	0.0511	0.0063
EDUL Dr23-2-5	0.0099	0.0190	0.0025	0.1296	[b]	0.0236	0.0014	0.247	0.006	0.0672	0.0092	0.260	0.008	0.0433	0.0072	0.390	0.012	0.0666	0.0039
EDUL Dr23-2-8	0.0059	0.0154	0.0043	0.0814	0.0227	0.0230	0.0021	0.180	0.037	0.0518	0.0014	0.183	0.016	0.0350	0.0022	0.277	0.015	0.0472	0.0044
EDUL Dr25-3-1		bdl		bdl		0.0089	0.0002	0.101	0.014	0.0334	0.0009	0.134	0.023	0.0267	0.0026	0.224	0.010	0.0413	0.0041
EDUL Dr23-3-2[d]		0.0093		0.0311		0.0083		0.088				0.091				0.202		0.0361	
EDUL Dr23-3-2		0.0455		0.1202		0.0248		0.195				0.176				0.253		0.0394	
EDUL Dr56-3-5	[b]	0.0037	0.0003	0.0376	0.0016	0.0086	0.0033	0.092	0.016	0.0389	0.0194	0.129	0.019	0.0271	0.0000	0.269	0.073	0.0424	0.0010
EDUL Dr56-3-11	0.0025	0.0048	0.0015	0.0554	0.0080	0.0132	0.0044	0.155	0.043	0.0509	0.0108	0.197	0.030	0.0348	0.0070	0.317	0.048	0.0517	0.0110
EDUL Dr69-1-1[e]		0.0426		0.0336				0.034				0.048				0.067		0.0110	
EDUL Dr69-1-1	0.0001	0.0008	0.0001	0.0136	0.0001	0.0051	0.0002	0.049	0.006			0.078	0.007			0.133	0.005	0.0206	0.0034

[a]Compositions are averages of porphyroclast cores, except specified. N, number of analyses; SD, standard deviation; bdl, below detection limit. Empty values mean not measured.
[b]Only one measure above detection limit.
[c]Only one measure.
[d]Measured near a clinopyroxene exsolution.
[e]Exsolution lamella in clinopyroxene.

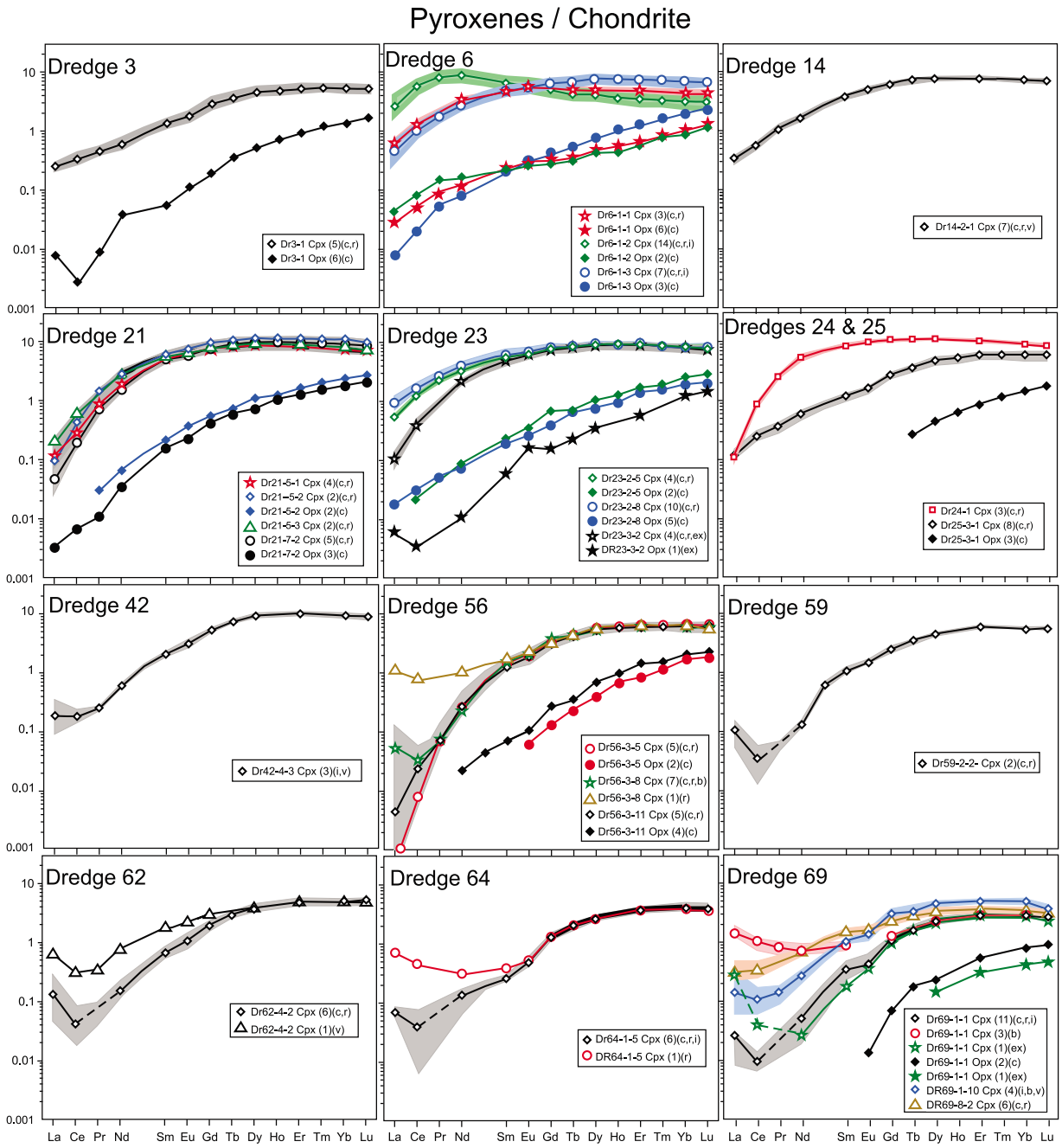

Figure 2. Chondrite-normalized pyroxene rare earth element patterns of EDUL peridotites dredged east (dredge sites Dr3–Dr25) and west (dredge sites Dr42–Dr69) of the Melville fracture zone. Each pattern averages several pyroxene textural types when variations are within analytical errors. The number of analyses is reported in legend, followed by the textural types: porphyroclast cores (c) and rims (r), interstitial grains (i), small, twinned clinopyroxene grains that grew on coarse orthopyroxene (b), veinlets (v), and exsolutions (ex). Grey fields represent the clinopyroxene compositional range for each sample (no field means that the variation is too small to be represented at the plot scale). Chondrite C1 concentration values are given by *Anders and Grevesse* [1989].

grain at thin section and sample scales. All the samples but Dr6-1-2 have Cpx depleted in LREEs relative to the MREEs and HREEs (Figure 2). Based on the shapes of their REE patterns, the eastern samples have been divided into four groups. Group E1 (six samples out of fourteen: Dr21-5-1, Dr21-5-2, Dr21-5-3, Dr21-7-2, Dr23-3-2, Dr24-1) characterized by near-flat HREE

contents at Yb_N = 8.9 ± 1.4 and moderate depletions in MREEs (Sm_N/Yb_N = 0.68 ± 0.15) and LREEs (Ce_N/Yb_N = 0.05 ± 0.03). These compositions are situated at the very fertile end of the spinel peridotite array sampled at mid-ocean ridges, and they fall in the compositional range characteristic of ultraslow spreading/cold ridges, such as the Vulcan fracture zone in the western SWIR [*Johnson et al.*, 1990] and the Lena Trough in the Arctic Ocean [*Hellebrand and Snow*, 2003]. The slopes defined by the most incompatible REEs are regularly decreasing toward lighter REEs, except in Dr21-5-1 Cpx that shows a small, preferential enrichment in LREEs. Group E2 (four samples out of fourteen: Dr6-1-3, Dr14-2-1, Dr23-2-5, 23-2-8) is distinguished by slightly lower HREE contents (Yb_N = 7.6 ± 0.7) and flatter MREE to LREE slopes, being less depleted in LREE/HREE (Ce_N/Yb_N = 0.15 ± 0.06) for similar depletion in MREE/HREE (Sm_N/Yb_N = 0.67 ± 0.10). Group E3 samples (two samples out of fourteen: Dr6-1-1, Dr6-1-2) have REE patterns that deviate from patterns typical of melting residues. In both samples Cpx have low HREE contents (Yb_N ~3–4). Cpx from Dr6-1-2 are characterized by convex-upward REE patterns with a maximum at Nd_N (~ 9) and (Ce_N/Yb_N) ~2. Dr6-1-1 is intermediate between Dr6-1-2 and Dr6-1-3. Group E4 (two samples out of fourteen: Dr3-1, Dr25-3-1) are the most depleted of the eastern sample set, with flat HREE contents starting at Yb_N = 5–6 and almost linear depletion in MREEs to LREEs (Sm_N/Yb_N ~0.25; Ce_N/Yb_N = 0.04–0.07; Ce_N/Sm_N = 0.22–0.26).

[18] West of the Melville fracture zone, the majority of the Cpx grains are also unzoned, with LREE-depleted compositions generally homogeneous within individual sample. However, a local variability is marked by preferential enrichments in La ± Ce that vary in amplitude within individual grains, a feature frequently reported in depleted Cpx from abyssal peridotites, and the occurrence of a few LREE-enriched compositions. LREE-depleted Cpx are more depleted than eastern samples and display a larger range of depletion, with Yb_N varying from 3 to 9 (Figure 2). REE patterns are typical of abyssal peridotites, with near-flat HREEs and strong depletion in LREE/HREE (Ce_N/Yb_N = 0.09 ± 0.07). Cpx compositions from dredge Dr42 harzburgite are the least depleted in REEs. Going westward, Cpx compositions of dredges Dr56 to Dr64 appear more depleted, comparable with the compositions of the Cpx from the Bullard fracture zone peridotites in the western SWIR [*Johnson et al.*, 1990]. The most depleted Cpx of our sample set are from dredge Dr69; they are as depleted as the Cpx of the Bouvet fracture zone peridotites, which have been shown to represent the most refractory samples of the entire SWIR [*Johnson et al.*, 1990; *Brunelli et al.*, 2003]. In contrast, the Cpx analyzed in the pyroxenite Dr69-8-2 have typical MORB-like, LREE-depleted pattern, with $(Ce/Yb)_N$ ~0.10 for Yb_N ~3–4.

[19] The enriched compositions have distinct preferential enrichments that start in the MREEs (Eu) and increase toward La, thus defining spoon-shaped REE patterns (Figure 2). These LREE-enriched compositions, observed in samples Dr56-3-8, Dr62-4-2, Dr64-1-5, Dr69-1-1 and Dr69-1-10, coexist with LREE-depleted compositions in the same thin section and even in the same grain. Spoon-shaped REE patterns may be observed on the rim but not in the associated core of some porphyroclasts. However, there is no true zoning because such Cpx grains are enriched asymmetrically, with spoon-shaped REE patterns characterizing only one side of the rim. In Dr69-1-1, spoon-shaped REE patterns characterize Cpx grains showing magmatic twins that grew replacing Opx [*Seyler et al.*, 2003, Figure 4G], whereas in Dr62-4-2 this feature is present in Cpx forming a veinlet that cuts through a coarse Opx grain. Despite their LREE enrichments, the Cpx having spoon-shaped REE patterns have the same HREE contents as the LREE-depleted Cpx in the same samples, suggesting that the process responsible for LREE enrichment did not affect the less incompatible elements.

[20] In all samples, both west and east of the Melville fracture zone, the concentration of the most incompatible elements (Sr, Nb, Zr) increases with increasing LREEs in Cpx. West of the Melville fracture zone, Sr contents of Cpx increase from group E1 through group E2 to group E3, whereas Sr contents in group E4 Cpx are as low as in group E1 (Figure 3a). The Cpx west of the Melville fracture zone, which have no or very low LREE re-enrichments, also show Sr contents (0.5–3.8 ppm) that increase with Ce contents, but the correlation is shifted to lower Ce/Sr for similar Sr contents (Figure 3a). Cpx from the pyroxenite Dr69-8-2 falls within Group E1 compositions. Although enriched in LREEs, Cpx with spoon-shaped REE patterns have Sr contents similar to those measured in the LREE-depleted Cpx in the same sample, and are thus characterized by higher Ce/Sr ratios and lower, generally negative, Sr/Sr* (where $Sr^* = (Ce_N.Nd_N)^{1/2}$); they plot within, or close to, the compositions of the eastern samples

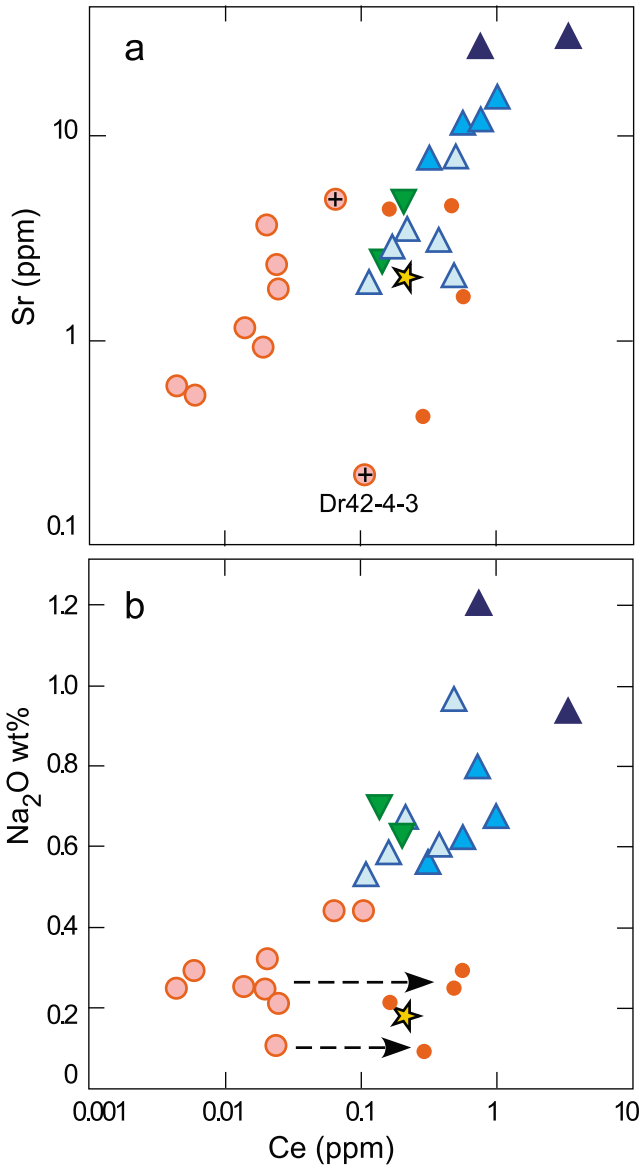

Figure 3. Sr and Na_2O versus Ce contents in clinopyroxenes of peridotites from the EDUL section of the SWIR. Triangles represent samples east of the Melville fracture zone: group E1 (light blue), group E2 (blue), group E3 (dark blue), and group E4 (inverted green triangles). Pink circles are samples west of the Melville fracture zone; a cross within a circle represents patterns characterized by a Ce rebound (Figure 2). Small orange circles are clinopyroxenes with spoon-shaped REE patterns. The star represents the pyroxenite from dredge Dr69. Arrows in Figure 3b indicate that Ce but not Na increases in Cpx showing spoon-shaped REE patterns, with respect to other Cpx in the same samples.

(Figure 3a). Dr42-4-3 Cpx show a weak preferential enrichment in LREEs, hence they are strongly depleted in Sr, with Sr/Sr* as low as 0.1, and plot at the most depleted end-member in Figure 3a. To discard a plagioclase effect on the lowest Sr contents we carried out a careful examination with optical and scanning electron microscopes, and found no traces of plagioclase or its alteration products. These strong negative Sr anomalies are observed in Cpx with no Eu anomaly and occur in plagioclase-free peridotites. Such strong negative Sr anomalies associated with anomalous LREE/HREE enrichments were also observed in some ODP Hole 1274 spinel harzburgites [*Seyler et al.*, 2007] and in peridotites from Saint Paul's Rocks in the Atlantic Ocean [*Brunelli and Seyler*, 2010]. *Parkinson et al.* [1992] and *Rampone et al.* [1996] have suggested that the

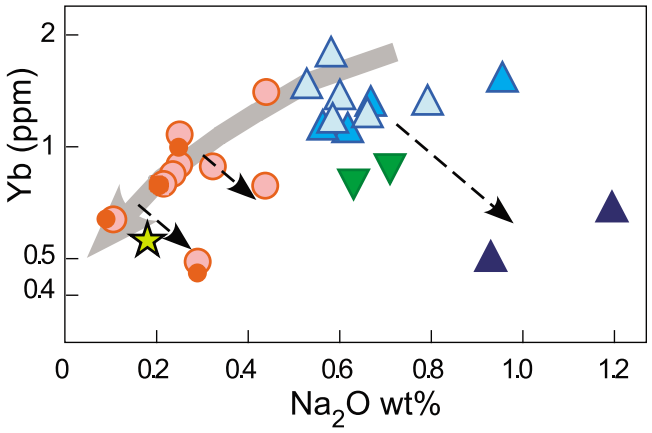

Figure 4. Yb versus Na_2O contents in clinopyroxenes of peridotites from the EDUL section of the SWIR. Symbols are the same as in Figure 3. The large gray array is the trend of increasing partial melting extent. Dashed arrows (enrichment in Na associated with depletion in Yb) might be interpreted as an effect of interaction between residual peridotite and low-degree, garnet-derived melt. Cpx with spoon-shaped REE patterns have similar Na and Yb contents than the other Cpx in the same samples.

incompatibility of Sr relative to the REEs might change depending on the melting (or enrichment) conditions, resulting in apparent negative or positive Sr anomalies when plotted using diagrams based on standard orders of incompatibility.

5.2. Correlations Between Major and Trace Element Compositions in Clinopyroxenes

[21] Na_2O contents in Cpx are positively correlated with concentrations in incompatible elements, but two groups of Cpx show different behaviors. First of all, Cpx with spoon-shaped REE patterns are enriched in Ce but not in Na_2O with respect to the LREE-depleted Cpx in the same samples (Figure 3b). Second, group E3 Cpx have low Yb contents (Figure 4) although they are strongly enriched in Na_2O (with ~1.2% Na_2O, they are among the Na_2O-richest Cpx known in abyssal peridotites). Group E4 Cpx and Cpx from dredge Dr69 also appear to be depleted in Yb and enriched in Na_2O.

[22] The major element characteristics of minerals, such as Cr# [= Cr/(Cr + Al)] of spinel, have been found to correlate negatively with Yb content in Cpx of abyssal peridotites [*Hellebrand et al.*, 2001]. A similar negative correlation between Cr# in Cpx, which has been shown to correlate with Cr# in spinel [*Seyler et al.*, 2003], and Yb is observed in EDUL samples (Figure 5a). Samples east of the Melville fracture zone define a global trend of decreasing Yb contents and increasing Cr# from group E1 through group E2 to group E3 samples. Group 4 samples plot on the same trend. Cpx west of the Melville fracture zone follow a similar trend but shifted to slightly lower Yb contents, with the exceptions of Dr42-4-3 and Dr69-1-10 Cpx that plot well above this trend. Figure 5a shows that the most refractory sample (harzburgite Dr69-1-1) and the most fertile sample in terms of cpx mode and enrichments in highly incompatible elements (lherzolite Dr6-1-2) have similar Cpx Yb content and Cr#. Figure 5b shows that both Na_2O and Cr# of Cpx increase from Group E1 through Group E2 to Group E3. Group E4 Cpx are also significantly enriched in Na_2O with respect to their Cr#, and plot on the trend defined by the groups E2–E3. Similar behavior can also be observed within dredge Dr69. In Figure 5b, only three dredges contain peridotites that fall on the trend of residual abyssal peridotites in general; they are samples from dredges Dr56, Dr62 and Dr64. Na_2O and Cr# compositions of the Cpx with spoon-shaped REE patterns are similar to the compositions of the LREE-depleted Cpx in the same samples.

5.3. Trace Element Compositions of Orthopyroxenes

[23] Trace element concentrations measured in porphyroclast cores are constant, within analytical accuracy, on grain and sample scales for the HREEs (Dy to Lu), Y and Ti, but dispersed for the most incompatible elements (LREEs and Sr) particularly in the most depleted samples (Dr3-1 and Dr25-3-1, Dr56 and Dr69 peridotites), for which

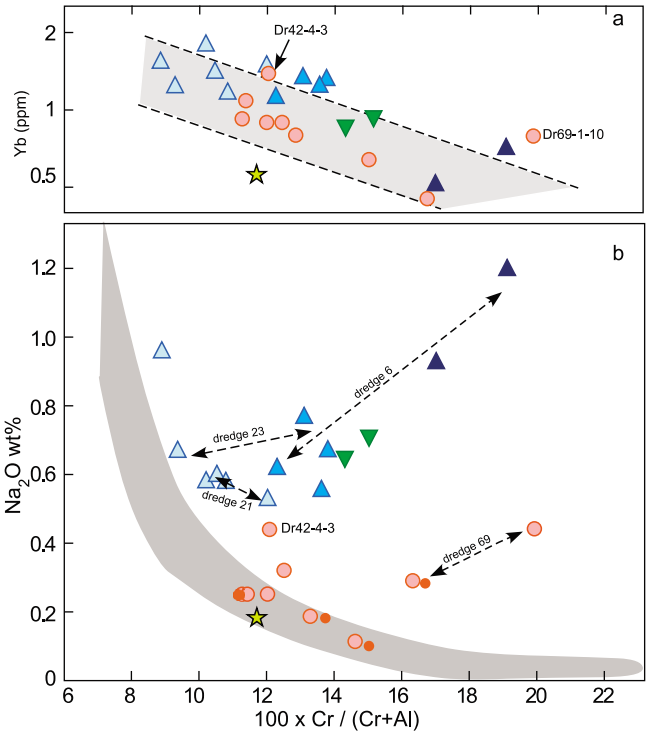

Figure 5. Yb and Na_2O versus Cr number in clinopyroxenes of peridotites from the EDUL section of the SWIR. Color grouping is the same as in Figure 3. (a) Gray field represents Cpx compositions of the abyssal spinel peridotite set of *Hellebrand et al.* [2001]. (b) Gray field represents Cpx of abyssal spinel peridotites with the lowest Na_2O contents (compilation of *Seyler et al.* [2003]). Arrows in Figure 5b show evolution trends within individual dredges.

concentrations approach the detection limit. C1-normalized REE patterns are typical of Opx from abyssal peridotites, i.e., characterized by linear decreases from HREEs to LREEs (Figure 2).

[24] East of the Melville fracture zone, Opx REE concentrations (average sample compositions) behave the same way as those of coexisting Cpx. HREE contents range between 1.7 and 2.4 in groups E1 and E2 Opx, but REE slopes are steeper in group E1 Opx [$(Ce/Yb)_N$ = 0.003–0.006)] than in group E2 Opx [$(Ce/Yb)_N$ = 0.009–0.017)]. Group E3 Opx have the lowest HREE contents (Yb_N ~0.9) with relatively flat REE patterns [$(Ce/Yb)_N$ = 0.053–0.100)]. Group E4 Opx have lower Yb_N (1.3–1.4) than Group E1 and E2 Opx but the REE slope is steeper in Dr3 (not measurable in Dr25-3-1), consistent with the more depleted compositions of their Cpx. West of the Melville fracture zone Opx are in general more depleted than Opx from the eastern samples, with Yb_N ranging from 0.8 to 1.9. They also have steeper Yb-Lu slopes whereas MREE and LREE concentrations are below or close to detection limits.

5.4. Orthopyroxene-Clinopyroxene Trace Element Partitioning

[25] REE partitioning between Opx and Cpx ($D_{opx/cpx}$) in mantle-derived peridotites have been shown to decrease with decreasing temperature [*Witt-Eickschen and O'Neill*, 2005; *Lee et al.*, 2007]. As a consequence, trace elements are expected to be redistributed among the peridotite minerals as the residual mantle crosses the thermal boundary layer. Because the trivalent REEs are likely to replace Ca^{2+} in the pyroxene M2 site, the Ca-Mg exchange reaction during subsolidus cooling exerts a control over REE partitioning between Opx and Cpx [*Witt-Eickschen and O'Neill*, 2005; *Lee et al.*, 2007]. Pyroxenes in abyssal peridotites show abundant exsolutions of the other pyroxene phase, indicating disequilibrium that may lead to incorrect estimates of the REE contents [*Agranier and Lee*, 2007]. EMPA CaO contents analyzed with a defocused beam (averages of several spots of 10 μm diameter) are slightly higher than those analyzed with LA-ICP-MS (single spot of 120 μm diameter) in the same grain (22.0 ± 0.8 wt% and 20.0 ± 1.7 wt%, respectively, for the 10 samples analyzed with both techniques). However, we have

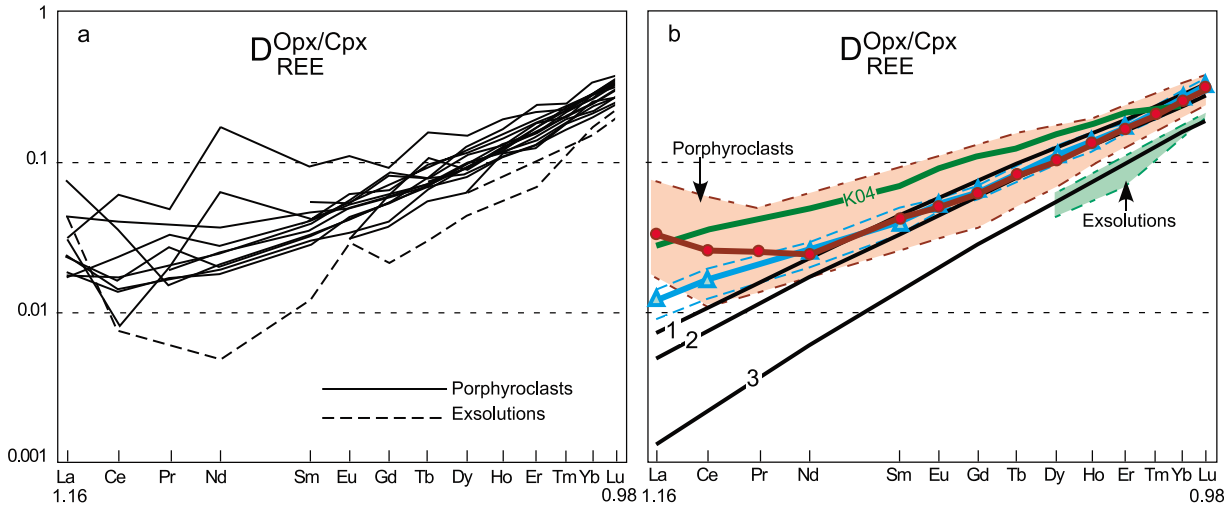

Figure 6. Partitioning of the REEs between orthopyroxenes and clinopyroxenes as a function of REE^{3+} radii (Å) in clinopyroxene. (a) EDUL samples are averages of orthopyroxene porphyroclast cores/clinopyroxenes for 14 samples and orthopyroxene exsolution/clinopyroxene host for 2 samples. (b) Red thick line with circles is average of EDUL samples (the two high Nd values are excluded). Blue thick line with triangles is average of the high-temperature (~1200°C) peridotite xenolith group of *Witt-Eickschen and O'Neill* [2005]. For both peridotite sets, fields limited by minima and maxima ratios are shown as dashed lines. Thick lines numbered 1, 2, and 3 are equilibrium partition coefficients calculated by *Agranier and Lee* [2007] for spinel peridotites at 1400°C, 1300°C, and 1000°C, respectively. Green thick line K04 represents *Kelemen et al.* [2004] partition coefficients in spinel peridotites at solidus temperature. Cationic radii are from *Shannon* [1976]. The large range of $D^{Opx/Cpx}$ in EDUL samples appears to be a function of the CaO content in orthopyroxene (see text).

shown above that the trace element concentrations in the Cpx measured with SIMS and LA-ICP-MS are similar within analytical accuracy, although the two techniques analyze different volumes of material, thus integrating different amounts of Opx exsolutions. As shown by *Hellebrand et al.* [2005], the REE concentrations in Cpx are thus high enough to not be significantly affected by the exsolution process. In Opx, EMPA CaO contents average 1.4 ± 0.3 wt% while LA-ICP-MS concentrations average 1.7 ± 0.3 wt%. Sample Dr23-2-8 is exceptional in that the CaO content of the grain analyzed by LA-ICP-MS (1.45 wt%) differs considerably from the CaO content of the grain analyzed by SIMS (1.05 wt%). As for Cpx, Opx trace element compositions measured with both techniques in the same sample do not differ significantly, although the SIMS analyses tend to be more scattered, with slightly lower REE concentrations. Average temperatures calculated with the Ca-in-Opx geothermometer of *Brey and Köhler* [1990] indicate that the compositions measured in the porphyroclast cores represent subsolidus compositions. The calculated temperatures are 1118 ± 56°C (EMPA) and 1185 ± 55°C (LA-ICP-MS) at P = 1 GPa and 1145 ± 57°C (EMPA) and 1214 ± 56°C (LA-ICP-MS) at P = 1.5 GPa.

[26] Apparent subsolidus $D_{opx/cpx}$ were calculated by dividing REE concentrations in Opx by REE concentrations in Cpx (C_{opx}/C_{cpx}). Following *Witt-Eickschen and O'Neill* [2005] and *Lee et al.* [2007], results are plotted as a function of effective cationic radii in Cpx, assuming all REEs are in eightfold coordination (Figure 6). The resulting trends vary from near-straight lines with negative slopes from Lu to La, to U-shaped curves, caused by progressive divergence in more incompatible REEs. Scattering also increases for MREE and LREE ratios in more depleted samples whereas C_{opx}/C_{cpx} in less depleted samples show relatively smooth variations with progressively varying cationic radii. In the whole set, C_{opx}/C_{cpx} (porphyroclasts) show 12–14% variations for Lu to Tm, 21–22% for Er to Dy, 27–32% for Tb and Gd, 41–46% for Pr to Eu, except a 100% variation for Nd, and 58–68% for Ce and La. In conclusion, all the LREEs are probably disturbed and will not be discussed further. When the MREEs and HREEs are considered, the lowest C_{opx}/C_{cpx} ratio (Dr 56-3-5) corresponds to the lowest Opx CaO content, while the highest C_{opx}/C_{cpx} ratios (Dr56-3-11 and Dr62-3-9) correspond to the highest Opx CaO contents. No difference is observed when comparing the different sample groups.

Table 4. Extents of Partial Melting Estimated From Heavy Rare Earths (Eu-Yb) Contents in Clinopyroxenes and Coexisting Spinel Compositions[a]

Sample	F% Grt[b]	F% Sp[b]	Total F%[b]	F% Sp[c]
EDUL Dr3-1	5	11	16	9.2
EDUL Dr6-1-3	0	8	8	7.5
EDUL Dr14-2-1	0	11	11	9.6
EDULDr21-5-1	0	7	7	5.0
EDUL Dr21-5-2	6	2	8	6.0
EDUL Dr21-5-3	3	7	10	6.1
EDUL Dr21-7-2	5	5	10	7.8
EDUL Dr23-2-5	3	7	10	9.6
EDUL Dr23-2-8	3	8	10	10.7
EDUL Dr23-3-2	3	8	11	4.8
EDUL Dr24-1	2	3	5	5.1
EDUL Dr25-3-1	6	11	17	9.4
EDUL Dr42-4-3	9	6	15	9.1
EDUL Dr56-3-5	7	8	15	7.3
EDUL Dr56-3-8	5	10	15	7.0
EDUL Dr56-3-11	6	9	15	6.4
EDUL Dr59-2-2[d]	6	12	18	9.2
EDUL Dr62-4-2	6	12	18	9.1
EDUL Dr64-1-5	7	12	19	10.6
EDUL Dr69-1-1[d]	4	19	23	12.7
EDUL Dr69-1-10[d]	5	17	22	16.3

[a]Caculations were performed assuming perfect fractional melting, depleted lherzolite source and polybaric melting parameters of *Brunelli et al.* [2006].
[b]Degrees of melting in the garnet and spinel fields and total degree of melting, respectively.
[c]Degrees of partial melting calculated with coexisting spinels [*Seyler et al.*, 2003] using *Hellebrand et al.*'s [2001] relation.
[d]Samples for which the shape of the measured HREE patterns are reproduced but shifted toward higher REE concentrations.

[27] HREE and MREE distribution curves for EDUL samples plot close to the high-temperature end of *Witt-Eickschen and O'Neill*'s [2005] data set for xenoliths. This result is not surprising, since CaO content of Opx's in EDUL peridotites, and temperatures calculated with the same geothermometer, are within the range of those characterizing the high-T group studied by *Witt-Eickschen and O'Neill* [2005]: CaO = 1.49–1.76 wt%; T = 1150–1250°C. The EDUL distribution curves for the HREEs (Lu to Gd) are also similar to those calculated by *Lee et al.* [2007] and *Agranier and Lee* [2007] at high temperatures (1300°C–1400°C) based on the elastic strain theory and peridotite partial melting experiments. These estimated temperature suggest that C_{opx}/C_{cpx} ratios for the MREEs and HREEs measured in EDUL peridotites are close to REE partitioning at the solidus-subsolidus transition in the thermal boundary layer. As shown by *Agranier and Lee* [2007], C_{opx}/C_{cpx} for the LREEs indicate that equilibrium on the mineral scale is not achieved for the most incompatible trace elements in abyssal peridotites with respect to peridotite xenoliths, even when only mineral cores are considered. The sample closest to equilibrium is also the most enriched sample, Dr6-1-2, in agreement with observations of *Agranier and Lee* [2007].

6. Discussion

6.1. Degree of Melting

[28] All peridotites but two (Dr6-1-1; Dr6-1-2) have Cpx trace element compositions within the range of residual mantle peridotites, characterized by LREE-depleted patterns. The relatively good overall correlation of Yb versus Cr# in Cpx (Figure 5a) along with the strong correlation of Cpx and spinel Cr# shown by EDUL rocks [*Seyler et al.*, 2003], allows the use of Cpx composition to estimate the degree of melting [*Hellebrand et al.*, 2001]. In this way we have estimated the apparent degree of melting of each sample based on the HREE contents in Cpx, assuming a homogeneous depleted MORB mantle source (DMM), and a near-fractional melting process following the experimental geometry and melting parameters of *Hellebrand et al.* [2002a] and *Brunelli et al.* [2006]. Results (Table 4) show that, although strongly variable, the samples west and east of the Melville fracture zone define two different degrees of melt extraction: 15–23% total melting and 5–17% total melting, respectively. Estimated degrees of partial melting are broadly anticorrelated with the modal abundance of Cpx in the peridotites (Figure 7), supporting the assumption of a first-order correlation due to variable extent of melt extraction [*Jaques and Green*, 1980; *Dick and Bullen*, 1984; *Johnson et al.*, 1990].

[29] Following the approach of *Hellebrand et al.* [2002a] the role of garnet during partial melting has been derived from fractionation of MREEs and HREEs in Cpx. The compositions of EDUL Cpx plot on two major trends in a $(Sm/Yb)_N$ versus Yb_N diagram (Figure 8). A main broad trend (trend 1) starts with 4–5% melting in the garnet stability field, continuing with variable degrees of melting in the spinel stability field. I is defined by the eastern groups E1 *pro parte*, E4 and the western samples. This near-fractional melting trend is within the range previously reported for residual abyssal peridotites [*Hellebrand et al.*, 2002a; *Hellebrand and Snow*, 2003; *Brunelli et al.*, 2006; *Seyler et al.*, 2007; *Brunelli and Seyler*, 2010]. The second trend (trend 2) takes root in group E1 peridotites and shows an increase in $(Sm/Yb)_N$ at

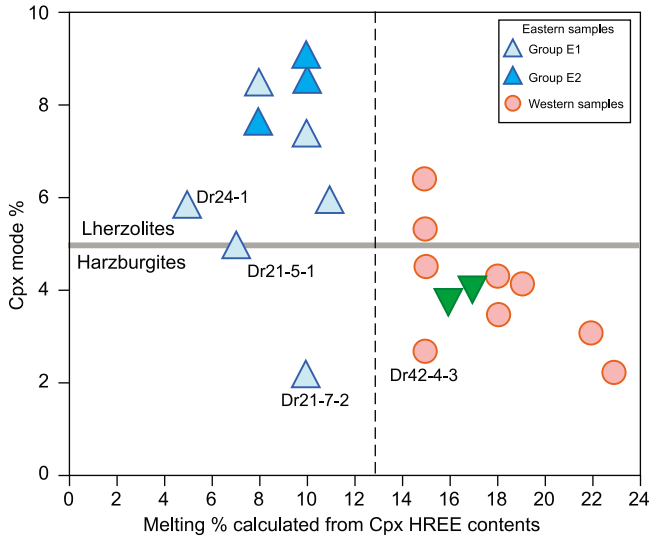

Figure 7. Modal abundance of clinopyroxene versus extent of melting estimated from the heavy rare earths contents in clinopyroxene. Calculations were performed using a fractional melting model with depleted lherzolite source and melting parameters of *Brunelli et al.* [2006]. Color grouping is the same as in Figure 3.

decreasing Yb_N, through group E2 to group E3 peridotites. This evolution is paralleled by the progressive enrichment in Na_2O, LREEs, Sr (Figure 4) and other highly incompatible elements (Nb, Zr) and by progressive increase in Cr# (Figure 5). The three peridotite groups are randomly distributed in a restricted ridge region, between 62°E and 67°E, having no specific relation to exact locations. For example, groups E1 and E2 can be found in dredge Dr23, and groups E2 and E3 in dredge Dr6, that gives evidence for processes acting at short length scales (<1 km).

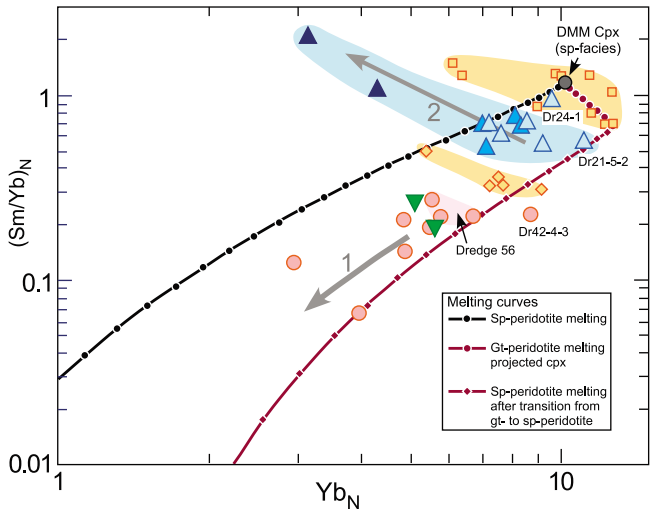

Figure 8. Variations of $(Sm/Yb)_N$ versus Yb_N in clinopyroxenes. Color grouping is the same as in Figure 3. Black curve represents model fractional melting trend in the spinel stability field, and brown curve is the spinel-equilibrated fractional melting trend after 7% melting in the garnet field followed by melting in the spinel field. Ticks marks are 1% melting steps. Arrow 1 indicates increasing degree of partial melting. Symbols for the EDUL samples are as in Figure 3. Arrow 2 within the blue field represents groups E1-E2-E3 sample array. Sample Dr24-1 plots off this field. The pink field encircles dredge Dr56 samples. Abyssal peridotites dredged in two locations, dredge VAN7-96 (squares) and dredge Van7-85 (diamonds), along the oblique amagmatic 9°E–16°E segment of the SWIR (yellow fields) are plotted for comparison (data from *Warren et al.* [2009]).

6.2. East of the Melville Fracture Zone

6.2.1. Group E1-E2-E3 Peridotites

[30] Hump-shaped REE patterns close to that of Dr6-1-2 Cpx are scarce in abyssal peridotites. They have been observed in the Central Indian Ridge (sample CIRCE 93-7 [*Hellebrand et al.*, 2002a]) and in the Arctic Ocean [*Hellebrand and Snow*, 2003]. In both occurrences, the peridotites are harzburgites very depleted in Cpx (0.1% modal cpx in CIRCE 93-7) and their peculiar REE patterns have been explained by refertilization with a depleted melt. Modeling by *Hellebrand et al.* [2002a] shows that entrapment and crystallization of a small amount of refractory melt in depleted harzburgites has the effect of significantly increasing Sm/Yb while keeping Yb very low and almost constant. With increasing refertilization, Sm/Yb starts to decrease whereas Yb increases. This effect produces a trend of inverse correlation between Sm/Yb and Yb, resembling EDUL trend 2, with the most refertilized samples having the highest Yb content and the lowest Sm/Yb ratio [*Hellebrand et al.*, 2002a, Figure 9]. Such behavior results from the low modal abundance of Cpx relative to Opx, the latter being the major phase controlling bulk distribution coefficients [*Hellebrand et al.*, 2002a]. Instead, EDUL peridotites are lherzolites (sample Dr6-1-2 contains ~10% modal Cpx) and EDUL cpx with the highest Yb content and the lowest Sm/Yb ratio plot on the global trend of residual compositions (trend 1). Modeling shows that refertilization of lherzolites with a depleted melt has the effect of increasing both Yb and Sm/Yb [*Hellebrand et al.*, 2002a], thus defining a trend opposite to that of EDUL trend 2. Finally, EDUL Dr6-1-2 has a $(Sm/Yb)_N$ twice that of CIRCE 93-7 for similar Yb_N, excluding refertilization by entrapment of depleted melt. A model of refertilization of residual lherzolites by entrapment of a LREE-enriched alkali melt could explain the positive correlation between the strong enrichments in LREEs and Na_2O, but in this case Yb is also expected to increase [*Hellebrand and Snow*, 2003]. In addition, refertilization by melt retention will also have the effect to increase the Al/Cr ratio (due to the aluminous character of the aggregated melts relative to the residue) and the other incompatible element abundances in the peridotite. As a consequence, while it will reproduce the negative correlation between Cr# and HREEs (see Figure 5), the negative correlation between strongly and moderately incompatible elements and the positive correlation between Na_2O and Cr# (Figures 4 and 8) cannot be reproduced. Therefore, compositional variations observed among the peridotites sampled along the 62°E–67°E ridge section must reflect small-scale heterogeneous premelting mantle and/or an effect of the melting process itself.

[31] In order to clarify the exact nature of the enrichment processes we have calculated the compositions of the melts in equilibrium with Cpx and compared them to the compositions of the basalts recovered along the same EDUL section [*Meyzen et al.*, 2003]. Calculated melts in equilibrium with group E1 Cpx (Figure 9a) are too depleted in LREEs to be in direct equilibrium with the regional basalts, showing that these peridotites are residual after melting. In contrast, melts in equilibrium with group E2 Cpx (Figure 9b) fall within the compositional range of the regional basalts. Whereas the HREE concentrations of group E2 Cpx can be explained by moderate degrees of melting in the spinel stability field (8–11%; Table 4), their LREEs are too enriched to be fitted by near-fractional melting models, not even accounting for a large fraction of melt being retained in the residue, up to 2% in a dynamic melting scenario. An additional 0.5–1.2% re-enrichment with a fully aggregated melt is then required to match the entire REE patterns. This simple melting and melt retention scenario may also explain the apparent equilibrium with the regional basalts, as well the high fertility in terms of major elements. However, this scenario cannot link group 2 to group 1 Cpx nor either to group 3 Cpx as discussed in the previous paragraph.

[32] The convex-upward REE pattern observed in Dr6-1-2 Cpx is typical of Cpx in equilibrium with an alkaline magma [*Irving and Frey*, 1984; *Downes et al.*, 2004] and has no equivalent among the known EDUL basaltic compositions (Figure 9c), not even among all other basalts sampled along the SWIR. The composition of the equilibrated melt could be that of a melt in equilibrium with a garnet-bearing residue (similar to melt generated by 1% melting of a garnet equilibrated DMM), suggesting that a garnet-bearing lithology was present in the partially molten mantle beneath the SWIR. Such melt may have never reached the surface, being trapped in the peridotite, or representing a minor component of the regional MORBs.

[33] The equilibrium of the group E1 peridotites with depleted melts favors the interpretation of these rocks as being representative of mantle parcels that experienced "normal" melting, i.e., near-fractional melting in which melt extraction prevails. Therefore all compositional parameters such as the concentration of incompatible (REE), or compatible (Cr),

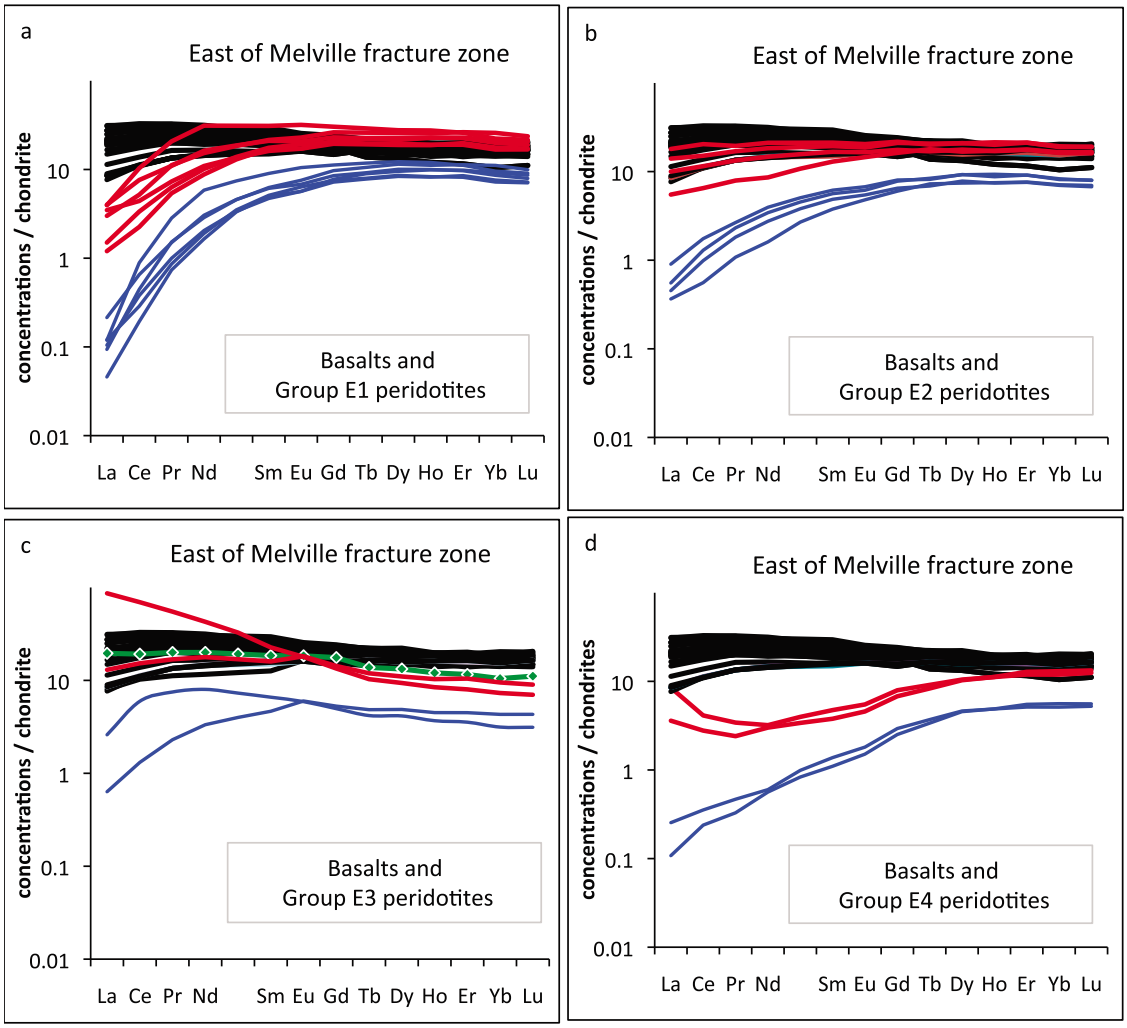

Figure 9. Chondrite-normalized REE patterns for the basaltic glasses (black) dredged east of the Melville fracture zone during the EDUL cruise [*Meyzen et al.*, 2003], the clinopyroxenes of the eastern peridotites (blue), and the melts in equilibrium (red) using partition coefficients of *Kelemen et al.* [2004]. In Figure 9c, the REE pattern of dredge Dr11 basalt is emphasized by diamonds.

elements are directly related to the total degree of melting as extensively discussed in the literature, even in the case of a small amount of melt retention in the residue. In fact the depleted nature of these melts cannot significantly modify the overall compositional fingerprint of the whole rock [*Brunelli et al.*, 2006]. For this reason group E1 can be assumed to be the closest to pure residual compositions and hence an acceptable starting point to test possible partial melting models for the region east of the Melville fracture zone.

[34] Four samples of group E1 peridotites were collected in the same dredge (Dr21); they show small compositional variations, with Cpx REE patterns varying in two different ways. First, Cpx of Dr21-5-1 and Dr21-5-3, on one hand, and Dr21-5-2 and Dr21-7-2, on the other, have near-parallel REE patterns, which cannot be attributed to different extents of melting (REEs fractionate during melting). The observed shift can be qualitatively explained by slightly different amounts of melt entrapment at the end of the partial melting event [*Hellebrand et al.*, 2002a; *Brunelli et al.*, 2006; *Brunelli and Seyler*, 2010]. Second, the Cpx REE patterns of the first pair of samples (Dr21-5-1 and Dr21-5-3) are slightly more depleted in HREEs and more enriched in LREEs than the second pair (Dr21-5-2 and Dr21-7-2), implying rotation of the REE patterns around the intermediate REEs (Sm-Gd). This rotation which links dredge Dr21 samples reproduces the rotation

which links dredge Dr6 samples (Figure 2), indicating that a similar process acts in both sites but with different amplitude. We have shown above that late-stage refertilization by entrapment of partially to fully aggregated melt cannot be responsible for the observed rotation.

[35] Melting of a lithological heterogeneity may severely influence the melting of the host mantle [*Kogiso et al.*, 2004; *Mazzucchelli et al.*, 2009; *Liang*, 2008]. However, to substantially affect the melting process it is necessary that the liquids produced by the melting heterogeneities are significantly different from those produced (or potentially produced) by the host mantle. For instance undersatured or oversatured silica melts may enhance pyroxene dissolution or force pyroxene crystallization. To address the origin of the E1-E2-E3 trend, a possible interaction to be considered is infiltration of garnet field–derived melt in a spinel field equilibrated mantle during melting. This scenario can be modeled by an open system melting approach where material influx can be accounted for.

[36] Open system melting with melt influx has been modeled by several authors (see *Shaw* [2000] and *Liang* [2008] for reviews). We base our work on the formulation of *Zou* [1998], who rewrote the equations proposed by *Ozawa and Shimizu* [1995] and the set of partition coefficients and melting modes of *Brunelli et al.* [2006]. The critical point is to define the mode and element composition of the mantle, and of the influxing melt. The simplest case is to consider that in a portion of mantle undergoing "normal" near-fractional partial melting the process converts to open system melting due to influx of a compositionally different melt. Upward movement of an enriched melt can be accompanied by focusing, thus affecting the percolated mantle to a very variable extent and ultimately resulting in juxtaposition of normal residual mantle with partially to strongly percolated rocks at all scales. This behavior is well illustrated at the outcrop scale where mantle rocks are exposed [e.g., *Mazzucchelli et al.*, 2009]. In our numerical experiment we have thus considered the starting point as the least HREE-depleted sample lying on a garnet-spinel melting path (sample Dr21-7-2). This sample can be generated by 5% melting in the garnet field followed by 5% melting in the spinel field and can be assumed as representative of the mantle prior to melt percolation. The best fit to the observed geochemical trends is then obtained by considering an enriched melt percolating through the rock in an open system setting with a finite residual porosity (0.5%) where 75% of the liquid filling the rock porosity is represented by the influxing melt that replaces the residual melt in equilibrium with the host rock. An additional 3% melting of the rock has been generated incrementally in this way. The behavior of the incompatible elements changes dramatically with respect to fractional melting with no melt influx because of the large influence of the incoming melt [*Ozawa and Shimizu*, 1995; *Liang*, 2008]. As reported in Figure 10a, a garnet field–derived partial melt induces a rotation around the position of Sm, resulting in the simultaneous decrease of the HREEs and increase of the LREEs (Figure 10b). The exact position of the rotation point is controlled by the composition of the infiltrating melt and to a lesser extent on the amount of melt infiltrating the rock. The LREE enrichment also depends on the geometry of the system, i.e., whether the addition of the incoming melt is continuous along the considered column or occurs as single pulses at the base of it [*Liang*, 2008]. This will result in a different modulation of the chromatographic efficiency of the melting column. Chromatography is in fact a component of any open system melting because of mass transfer through the cell sequence [*Liang*, 2008; *Liang and Peng*, 2010]. A complete discussion of this behavior is however beyond the scope of this paper and will be presented in a forthcoming contribution. The important thing to retain here is that rotation around a single REE may easily result from open system melting where the infiltrating melt is produced in the garnet stability field, as shown by *Ozawa and Shimizu* [1995]. Model results for a spinel field–derived partial melt influxing the melting peridotite are also reported in Figures 10c and 10d. It is noticeable that under the same conditions, the effect on the Sm/Yb ratio is much weaker, while HREEs are buffered at a constant value.

[37] This open system melting model with influx of garnet-derived melt satisfactorily explains the continuity of compositions of Cpx from group E1 through group E2 to group E3. This also explains that, in the same dredge, compositions apparently requiring initiation of melting in the garnet stability field coexist with compositions that can be modeled in the spinel stability field alone. In this model, the trace element composition of Dr6-1-2 is fully equilibrated with the influxing melt, which has for effect to imprint an OIB-like chemical signature untypical of abyssal peridotite but similar to those found in many xenoliths and massif lherzolites. Continuous flux of melt in the rock during open system melting is accompanied by enhanced local

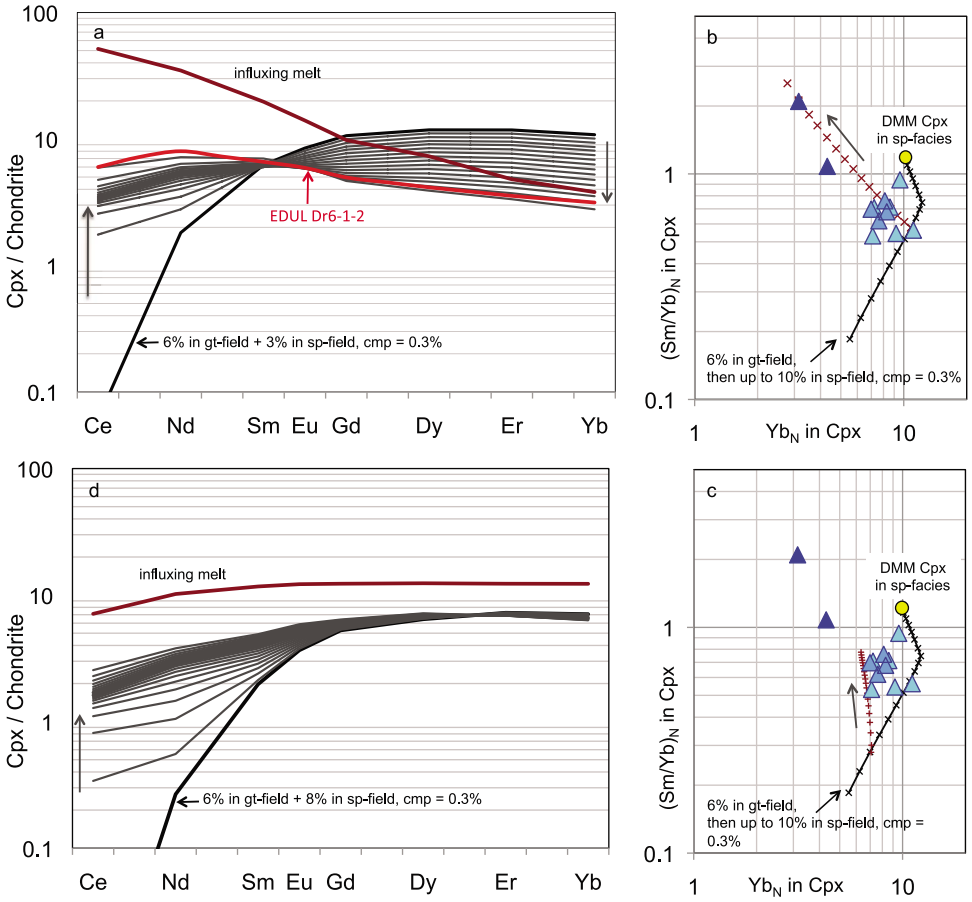

Figure 10. Compositional evolution of model residual clinopyroxenes during an open system melting event. The open system event is assumed to occur after a certain amount of near-fractional melting thus starting with a variably depleted source. Model compositions are plotted (a and c) as chondrite-normalized patterns and $(Sm/Yb)_N$ versus (b and d) $Yb_{(N)}$. Model residual clinopyroxenes in a peridotite after 9% partial melting (6% in garnet field + 3% in spinel field) for open system melting with influx of a garnet field–derived melt (Figures 10a and 10b). The melt fluxing the peridotite is assumed to be a 1% partial melt produced in the garnet field by a normal DMM. During open system, the HREEs are depleted while the most incompatible elements are enriched. Curves are each 0.25% melting. Model residual clinopyroxene in a peridotite after 14% partial melting (6% in garnet field + 8% in spinel field) (Figures 10c and 10d). Open system melting accounts for influx of a spinel field–derived melt. In both models the critical mass porosity (cmp) is set to 0.3%; the incoming/residual melt = 0.75. Arrows point to increasing degree of open system melting.

melting, which significantly increase Cr# in pyroxenes and spinel. Because compatible elements are retained and incompatible elements are leached according to their incompatibility and relative enrichment with respect to the influxing melt and the rock content, the negative correlation between Cr# and HREE is preserved (or enhanced) (Figure 5a) and concomitantly a negative correlation between the least and the most incompatible elements is generated (Figures 4 and 8). Na_2O (but not TiO_2 [*Seyler et al.*, 2003]) is also enriched because of the high diffusivity from the Na-rich melt and stability of jadeitic component at high pressure [*Blundy et al.*, 1995; *Lundstrom*, 2000], leading to a positive correlation between Cr# and Na_2O (Figure 5b).

[38] Our modeling suggests that the rate of melt influx is high compared to the rate of partial melting. Thus, local melt production is low and possibly only induced by the chemical instability due to the percolation of a compositionally different melt. Low melting and a high external melt fraction suggest that there is not enough heat to sustain robust local (spinel field) partial melting. In the context of very slow/cold mantle upwelling, a thicker than normal conductive layer may develop lowering the upper extension of the melting region, inhibiting melt extraction and favoring melt stagnation. In the peridotites that started melting in the garnet stability field, this process has the paradoxical effect of erasing the residual garnet signa-

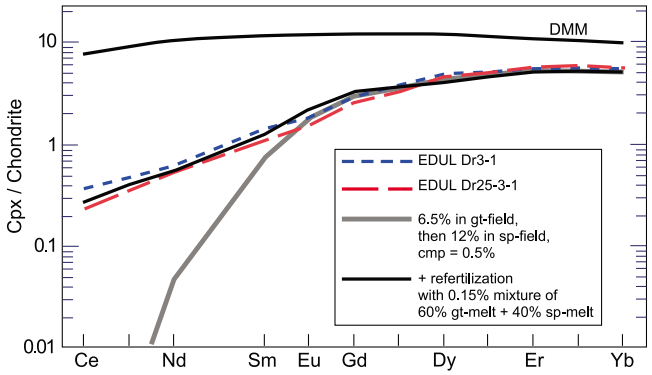

Figure 11. REE pattern modeling of group E4 clinopyroxenes (east of the Melville fracture zone). A two stage model is considered in which weak refertilization by a partially aggregated melt (mixing components from the garnet and spinel fields) occurs to a normally depleted source following the rationale of *Brunelli et al.* [2006].

ture, by decreasing Yb but increasing MREE and LREE/HREE ratios. Therefore, calculated residual compositions plot along trends that crosscut polybaric fractional melting trends.

[39] At a sample scale, refertilization by late-stage entrapment of enriched melts may nevertheless also account for part of the variability of the less incompatible REEs as well as modal variations among the eastern peridotite set, as shown by *Hellebrand et al.* [2002a] and *Brunelli et al.* [2006]. For example, Cpx REE patterns of Dr21-5-2 and Dr21-7-2 are parallel but the latter is shifted to higher overall REE contents; this sample likely followed a similar melting history to that of Dr21-7-2 before being refertilized by retaining a small amount of enriched melt at the end of the melting process. In a similar way, sample Dr24-1, the most fertile sample of this peridotite set, has a composition close to that of DMM that suggests low degree of melting (≤5%). At such a low depletion, the MREEs are not fractionated enough from the HREEs to assess the role of garnet in the melting process. However, we observe that the LREEs are quite depleted relative to the MREEs and HREEs (Figure 2). The overall shape of the Dr24-1 REE pattern is parallel to that of residual Cpx calculated after ~6% fractional melting in the spinel stability field, but is enriched in all the REEs. Entrapment of the last partial melt fraction at the end of the melting history is compatible with increased REE contents and low LREE/MREE ratio, but requires quite a large amount of trapped melt (~3%). This estimate is, however, consistent with the low pyroxene and spinel Cr#, silicate Mg# and high Cpx TiO_2 of this sample relative to the other samples (Table S1) [*Seyler et al.*, 2003].

6.2.2. Group E4 Peridotites

[40] Group E4 Cpx (Dr3-1 and Dr25-3-1) are significantly more depleted in REEs than the Cpx of the other samples east of the Melville fracture zone, but plot on the same near-fractional (closed-system) melting trends as Dr21-5-2 and Dr21-7-2 (Figures 8 and 10). Their high LREE contents and the peculiar linear decrease from MREE to LREE cannot be modeled by either pure fractional nor open system melting. Cpx HREE contents can be reproduced by 5–6% near-fractional melting in the garnet stability field followed by 10–11% melting in the spinel field of a DMM source, with residual porosity ≤0.5% (Table 4). To match the observed LREE trend refertilization with a melt generated across the garnet/spinel transition is needed even though its amount is low (up to 0.2%; Figure 11). This value is comparable to those estimated for the Vema fracture zone by *Brunelli et al.* [2006]. This kind of refertilization is different from the open system melting described in the previous section. Here, the case is that of a normal melting/extraction process where local addition of a melt fraction generated in the garnet field occurs during the late stages of melting or soon after while the residual porosity is still open (even though very small: < 0.2%). Again, this result suggests that garnet-derived melts play a major role in defining the composition of the peridotites from this stretch of the SWIR.

6.3. West of the Melville Fracture Zone

6.3.1. Normal LREE-Depleted Peridotites

[41] Western samples are more depleted than the eastern ones and clearly residual after melting. Still

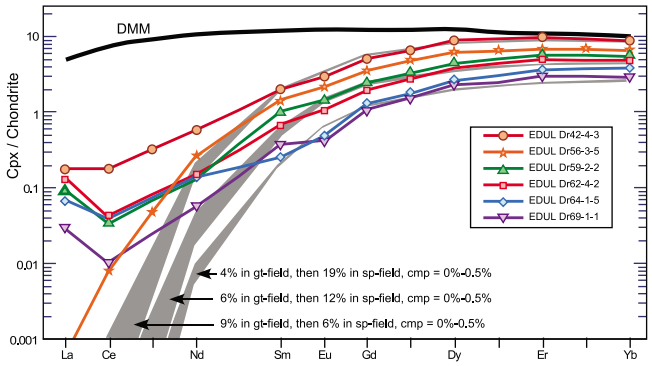

Figure 12. Models for samples located west of the Melville fracture zone. Residual clinopyroxenes (the three gray fields) are calculated using the polybaric melting model of *Brunelli et al.* [2006], with critical mass porosity (cmp) varying between 0 (pure fractional melting) and 0.5%. With respect to residual Cpx, all the Cpx need to be re-enriched in LREEs in a way similar to that suggested for group E4 samples (Figure 11) to explain the too flat Ce-Sm sections of the REE patterns. The La (+Ce in sample Dr42-4-3) rebound observed in five samples is explained by secondary, finer-scale chromatographic effects.

their LREE slopes are too flat with respect to the residual patterns of near-fractional (≤0.5% residual melt porosity) melting (Figure 12). The extents of melting calculated with the Cpx HREE contents in dredges Dr56, Dr62 and Dr64 (Table 4) fit reasonably well with the abundance of Cpx (Figure 7). The flat LREE slopes can be explained by addition of a melt enriched in REE before the end of peridotite melting [*Hellebrand et al.*, 2002a; *Brunelli et al.*, 2006; *Godard et al.*, 2008]. This melt may be a partially aggregated melt formed at a deeper level in the melting region or melt derived from a source heterogeneity. The Cpx from dredge Dr56 define a very short trend of decreasing Yb_N and increasing Sm_N/Yb_N (Figure 8) that suggests a possible influx of garnet-derived melt during peridotite melting.

[42] In contrast, the modeling of Cpx HREE contents in peridotites from dredges Dr42, Dr59 and Dr69 leads to inconsistent results. The Sm to Yb section of the Cpx REE pattern in Dr42-4-3 (Figure 12) can be fitted by 15% fractional melting (including 9% in the garnet stability field) leaving a lherzolite residue (4.6% Cpx) which contrasts with the low modal Cpx (<3%) content of this sample and that of the other harzburgites collected at this dredge haul. Increasing the degree of melting in the spinel stability field up to 19% leaves a residue whose modal composition fits the observed value (Figure 7), but the residual sample must have retained up to 1% of the last-degree melts to match the measured Sm-Yb concentrations. Similarly, Cpx modal proportions and relative MREE to HREE concentrations in samples from dredges Dr59 and Dr69 can be reproduced after 20% fractional melting (6% in the garnet stability field) for Dr59-2-2 and 22–23% fractional melting (4% in the garnet stability field) for Dr69-1-1 and Dr69-1-10. However, the calculated REE patterns are again shifted toward lower absolute REE concentrations, suggesting entrapment of aggregated melt in the upper part of the melting column.

6.3.2. Spoon-Shaped REE Patterns

[43] A few Cpx are characterized by over-enrichments in the most incompatible REEs superimposed on the LREE-depleted patterns and affecting the REEs more incompatible than Sm (Dr56), Eu (Dr64) or even Gd (Dr69) and Dy (Dr62). The resulting patterns have been described as spoon shaped. These spoon-shaped REE Cpx occur randomly and coexist in the same thin section with unzoned Cpx which show no or only weak inflections in La ± Ce. They are late-stage features, such as veinlets (Dr62) or part of the grain rims, thus reflect secondary processes operating at lower temperature in the lithospheric mantle. Na_2O content and other major element composition are not modified. These REE enrichments are easily modeled as cryptic metasomatism caused by chromatographic fractionation during postmelting elemental diffusion at some distance from melt channels transporting a MORB-type magma (e.g., the regional basalts). Applying trace element chromatographic exchange models developed in literature, the strong enrichments observed in the spoon-shaped Cpx can be accounted for by considering long percolation times or short distances from melt transport channels [cf. *Navon and Stolper*, 1987; *Bodinier et al.*, 1990; *Takazawa et al.*, 1992; *Batanova et al.*,

1998; *Godard et al.*, 2000; *Warren and Shimizu*, 2010]. Examples of such enhanced small-scale heterogeneities in the SWIR subridge mantle have been modeled by *Warren and Shimizu* [2010]. Based on calculations of the timescales for diffusive equilibration, *Warren and Shimizu* [2010] show that incomplete homogenization of the Cpx grains implies that metasomatism occurred relatively deep (≥10 km) in the lithosphere at 1000°C–1200°C. Our Cpx with spoon-shaped REE patterns display features similar to those studied by *Warren and Shimizu* [2010] (sporadic occurrences in vein-free, otherwise LREE-depleted samples; no change in major element chemistry) but differ by a more restricted range of compositional variation. Indeed, REE patterns usually associated with modal plagioclase (enrichments in all REEs including the HREEs and negative anomaly in Eu) are lacking, thus indicating that the metasomatic event(s) occurred before plagioclase saturation in the infiltrating melts or deeper than the spinel-plagioclase transition. Cpx with spoon-shaped REE patterns were not observed in the peridotite east of the Melville fracture zone.

6.4. Multiscale Heterogeneities

[44] Data of this study confirm the strong compositional heterogeneities of the residual lithospheric mantle that were predicted beneath ultraslow spreading/cold ridges and observed in other regions of the SWIR [*Johnson et al.*, 1990; *Johnson and Dick*, 1992; *Warren et al.*, 2009; *Warren and Shimizu*, 2010], at the Gakkel Ridge [*Hellebrand et al.*, 2002b] and in the Equatorial Atlantic [*Brunelli and Seyler*, 2010]. It is worth noting the contrast of compositions with the thick lithospheric mantle sampled in the 15°20′N region of the slow spreading Mid-Atlantic Ridge, also characterized by large outcrops of serpentinized peridotites and thin volcanic crust [*Kelemen et al.*, 2007]. There, percolating melts have stripped out the peridotite of its incompatible elements leaving homogeneous Cr-Mg rich harzburgites [*Seyler et al.*, 2007; *Godard et al.*, 2008]. In the SWIR, several stages of melt-peridotite interaction operating at small length scales mainly result in fertilization processes; heterogeneities are generated at different times and are superimposed on each other. We suspect that the study of a larger number of samples per dredge would have revealed a greater variability of the peridotite composition at this scale.

[45] Within-dredge heterogeneities observed in the EDUL sample set also show striking differences in magnitude and style with the within-dredge variability which characterizes mantle residua underlying normal oceanic crust in regions of the Mid-Atlantic Ridge. For instance, at the Vema fracture zone (MAR 11°N), the compositions of the peridotites sampled in a single dredge define single spinel-projected, near-fractional, partial melting trends starting in a restricted depth interval in the $(Sm/Yb)_N$ versus Yb_N diagram; the observed within-dredge variability can be interpreted in terms of a relatively large degree of decompressional melting in the spinel stability field slightly modified by late-stage refertilization during melt extraction and entrapment [*Brunelli et al.*, 2006]. On the contrary, EDUL samples collected in the same dredge show a stronger scatter in the estimated amount of garnet stability field melting. This would suggest these samples started melting at variable depths at a subkilometer scale, a conclusion inconsistent with mantle temperature distribution at depth and the hypothesis of a compositionally homogeneous source region. Our model points to a short melting column and melt/rock interaction occurring across, or close to, the garnet/spinel transition suggesting that melting may be confined between the thick/cold lithosphere and the spinel/garnet phase transition, possibly limiting the extent of melting itself [*Asimow et al.*, 1995]. Enhanced reaction at magmatic temperature with deep melts in compositional disequilibrium with the peridotite matrix results in REE patterns characterized by gently dipping LREE slopes that contrast with the strong LREE/MREE and LREE/HREE depletions observed in "normal" residual abyssal peridotites, such as those studied by *Johnson et al.* [1990]. The abyssal peridotites dredged along the axis of the central part of the SWIR (9°E–16°E) display large compositional variability similar to the EDUL samples [*Warren et al.*, 2009; *Salters and Dick*, 2002]. The central SWIR is characterized by long, oblique, amagmatic spreading segments [*Dick et al.*, 2003], with obliquity and thus effective spreading rate even more pronounced than in the region east of the Melville fracture zone, indicating lower melt supply and thick lithospheric mantle [*Cannat et al.*, 2008], in agreement with the basalt compositions [*Le Roex et al.*, 1983, 1992; *Standish et al.*, 2008]. In Sm_N/Yb_N versus Yb_N (Figure 8) and Ce_N/Yb_N versus Yb_N (not shown) diagrams, Cpx compositions of peridotites from two dredges, Van7-85 and Van7-96 [*Warren et al.*, 2009; *Salters and Dick*, 2002] define within-dredge trends parallel to the EDUL trend, crossing across spinel-projected near-fractional partial melting trends that start at variable depth intervals and extending toward increasing

enrichments in more incompatible REEs as Yb decreases. *Warren et al.* [2009] have shown the extreme isotopic variability of the peridotites of the central SWIR. Similar isotopic variability may be predicted in the abyssal peridotites east of the Melville fracture zone, reflecting a heterogeneous mantle source.

[46] Large compositional variations overprinted on the residual peridotites make it very difficult to assess the total degree of melting experienced by the peridotite during the last decompressional melting beneath the present-day ridge axis. The degree of melting estimated from crustal thickness is also subject to caution considering that magma can partly be generated by melting of pyroxenite or other heterogeneities. There is also evidence that melt produced over a large mantle region is delivered after focusing toward restricted areas of prominent volcanic centers, resulting in strong along-axis variability in the estimated crustal thickness [*Cannat et al.*, 2008]. Indeed, melting indicators in EDUL basalts and peridotites are poorly correlated [*Meyzen et al.*, 2003; *Seyler et al.*, 2003] (Table 4), as predicted by numerical flux melting models [*Liang*, 2008]. As shown by *Cannat et al.* [2008], lack of (or very thin) volcanic crust in the avolcanic oblique segments does not necessarily reflect very low melt supply from the underlying mantle, because the melts can propagate along axis toward adjacent volcanic segments [*Cannat et al.*, 2008; *Standish et al.*, 2008]. Nevertheless, this study indicates that peridotites west of the Melville fracture zone are systematically more depleted in incompatible trace elements than peridotites east of the Melville fracture zone, suggesting higher degrees of partial melting, in agreement with the wealth of data concerning this region of the SWIR. East of the Melville fracture zone, the highest fertility in terms of incompatible trace element contents, but also in terms of major element mineral compositions and Cpx mode [*Seyler et al.*, 2003], characterize the peridotite sampled at ~62°35′E (dredge Dr24); then the overall fertility decreases to both sides (toward dredge sites Dr3 and Dr25) to approach the depleted compositions west of the Melville fracture zone. However, this dome-like variation in the eastern region could be an artifact due to insufficient sampling. Alternatively, it could reflect a concentration of the heterogeneities in the source region around ~62°E.

6.5. Source Composition

[47] Nd-Sr isotopes in dredge Dr6 basalt suggest that a small proportion of an enriched component is present in its composition ($^{144}Nd/^{143}Nd$ = 0.51302, $^{87}Sr/^{86}Sr$ = 0.70312 [*Meyzen et al.*, 2005]), even though the trace element patterns lacks a clear "garnet" fingerprint [*Meyzen et al.*, 2003]. Basalts sampled in dredge Dr11 may help unraveling the correlation between peridotites and basalts in dredge Dr6. The anomalously (relative to other EDUL basalts) isotopically enriched composition of Dr11 basalts ($^{144}Nd/^{143}Nd$ = 0.51288, $^{87}Sr/^{86}Sr$ = 0.70362) is associated with a REE pattern (Figure 9c) showing a marked downward inflection toward the HREEs [*Meyzen et al.*, 2003, 2005]. This suggests that a phase retaining the HREEs (assumed to be garnet) was present in the mantle source, and that the garnet-bearing source produced melts with an enriched isotopic signature. In this case, however, the ratio between enriched component and depleted "normal" ambient mantle source is greater than for the Dr6 basalt where only the isotopic evidence is measurable. If we assume similar mechanisms for Dr6 and Dr11 (also supported by the character of melts in equilibrium with the Dr6 peridotites) we conclude that an enriched, garnet-bearing component was present in the upper mantle beneath this entire region of the SWIR although its signal is variably diluted in the erupted MORBs. Additionally, this observation demonstrates that deep partial melts can locally reach shallower levels throughout the melting column without significant mixing with more depleted melts produced at lower pressure, and also shows the ability of residual peridotites to preserve traces of these partial melts. This is possible in "a highly channelized melt transport system," which allows isolation of melts produced at different depths [*Spiegelman and Kelemen*, 2003]. Melting of enriched lithologies may itself promote the dissolution process ultimately leading to the development of a dunitic channel [*Mazzucchelli et al.*, 2009]. Hence, the apparent proportion of dunites recovered in dredge Dr6 is higher than in the other dredges [*Mével et al.*, 1997] and most of them contain a few insterstitial Cpx grains highly enriched in Na_2O (M. Seyler, personal data, 2009). Finally, this observation is consistent with a short melting column (small degree of decompressional melting) and a thick thermal lithosphere, which allows the preservation of the chemical signature of an early melting stage in the residual peridotite.

[48] Dredge Dr3 is located in the EDUL ridge region where basalts have isotopically enriched compositions. Nd-Sr isotopic composition of the Dr3 basalt also suggests the presence of a small proportion of an enriched component ($^{144}Nd/^{143}Nd$ = 0.51307, $^{87}Sr/^{86}Sr$ = 0.70290 [*Meyzen et al.*,

2005]). In contrast, Dredge Dr25 is located further to the west where the analyzed basalts are isotopically more depleted, extending from moderately enriched to DMM compositions. Dredge Dr25 delivered no fresh basalt but is located very close to dredge Dr26 on the same intersegment. Dr26 basalts have the most enriched compositions of this ridge section ($^{144}Nd/^{143}Nd$ = 0.51306 and $^{87}Sr/^{86}Sr$ = 0.70287 [*Meyzen et al.*, 2005]), similar to that of Dr3 basalt. Thus, similar LREE enrichments in Dr3-1 and Dr25-3-1 peridotite Cpx would suggest a link with the enriched component in the regional mantle.

[49] The region between the Gauss and Melville fracture zones is represented by basalts with normal MORB isotopic signatures, except at ~55°4′E where the dredge Dr57 basalt is isotopically similar to most eastern samples ($^{144}Nd/^{143}Nd$ = 0.51307 and $^{87}Sr/^{86}Sr$ = 0.70291 [*Meyzen et al.*, 2005]); these basalts form a volcano located on the same intersegment as the dredge Dr56. This suggests that the short trend of decreasing Yb_N and increasing Sm_N/Yb_N observed in the Cpx of Dr56 peridotites may also be connected with local isotopic enrichment, although this effect is much less marked in Dr56 peridotites than in the eastern peridotites.

[50] Source heterogeneities can be represented by pyroxenite veins as proposed by *Salters and Dick* [2002] or metasomatic enrichments of a previously depleted peridotite [*Warren et al.*, 2009; *Meyzen et al.*, 2005]. Adiabatic decompression of asthenospheric peridotite mantle previously contaminated by low-degree melts enriched in H_2O, alkalis and other incompatible elements may have triggered an early stage of partial melting in the garnet stability field, which could explain the garnet signature both in the residues and in the metasomatic melts. The discovery in dredge Dr23 of olivine-poor harzburgites enclosing in their Opx metasomatic minerals enriched in volatiles and incompatible elements supports the hypothesis of interaction between peridotite and low-degree melts prior to the generation of the regional MORBs [*Seyler et al.*, 2004].

7. Conclusions

[51] The easternmost SWIR region located east of the Melville fracture zone is characterized by relatively fertile mantle residues highly heterogeneous from the dredge scale down to the sample scale. Melting modeling suggests that this variability results from spinel field open system melting in presence of garnet-derived melts flowing through the peridotite. Retention of variable amounts of mixed (garnet- and spinel-derived) partially aggregated melts at the top of the melting column results in the observed short length-scale variability. Peridotite REE compositions attest for melt derived from a garnet-bearing lithology to be generated beneath the present-day ridge, the garnet fingerprint appearing as a diluted component in the regional basalts.

[52] West of the Melville fracture zone, the mantle appears more homogeneous at a local scale while effects of melt influx during melting are less important. We interpret this as resulting from a greater degree of melting of the peridotite in the spinel stability field. Enhanced melt production and extraction reduces the possible interaction with percolating melts thus better approaching the fractional end-member melting model.

[53] The observed heterogeneity differs in the two regions: high-frequency, strong heterogeneities in the region east of the Melville fracture zone deriving from strong melt-rock interaction in an open system melting with large influence of the incoming melt. In the western region the mantle residues are homogeneous at a larger, regional, scale while the melting style is more akin to the fractional melting with lower melt influx. These observations agree well with the different thermal setting estimated from bathymetry and geophysics [*Cannat et al.*, 2008] that reveal the eastern region to be characterized by oblique spreading and colder thermal setting.

[54] In both regions east and west of the Melville fracture zone, the peridotite compositions require initiation of melting in the garnet stability field. However, the garnet signature in residual clinopyroxenes was partially masked during the open melting process due to the progressive rotation of the REE patterns.

Acknowledgments

[55] We are grateful to Bernard Boyer for his assistance with the SIMS analyses and to Olivier Bruguier for technical assistance on the LA-ICP-MS. This paper benefited from constructive reviews by Elisabetta Rampone and an anonymous reviewer. Funding for this research was provided by Centre National de la Recherche Scientifique–Institut National des Sciences de l'Univers programs Dynamique et Evolution de la Terre Interne and Planétologie–Sciences de la Terre. DB has partially been funded by Fondazione Cassa di Risparmio di Modena through CARBRIDGE project. This is IPGP contribution 3196.

References

Agranier, A., and C. T. A. Lee (2007), Quantifying trace element disequilibria in mantle xenoliths and abyssal peridotites, *Earth Planet. Sci. Lett.*, *257*(1–2), 290–298, doi:10.1016/j.epsl.2007.02.041.

Ahern, J. L., and D. L. Turcotte (1979), Magma migration beneath an ocean ridge, *Earth Planet. Sci. Lett.*, *45*, 115–122, doi:10.1016/0012-821X(79)90113-4.

Anders, E., and N. Grevesse (1989), Abundances of the elements: Meteoritic and solar, *Geochim. Cosmochim. Acta*, *53*(1), 197–214, doi:10.1016/0016-7037(89)90286-X.

Asimow, P. D. (1999), A model that reconciles major- and trace-element data from abyssal peridotites, *Earth Planet. Sci. Lett.*, *169*, 303–319, doi:10.1016/S0012-821X(99)00084-9.

Asimow, P. D., M. M. Hirschmann, M. S. Ghiorso, M. J. O'Hara, and E. M. Stolper (1995), The effect of pressure-induced solid-solid phase transitions on decompression melting of the mantle, *Geochim. Cosmochim. Acta*, *59*(21), 4489–4506, doi:10.1016/0016-7037(95)00252-U.

Baines, A. G., M. J. Cheadle, H. J. B. Dick, A. H. Scheirer, B. E. John, N. J. Kusznir, and T. Matsumoto (2007), Evolution of the Southwest Indian Ridge from 55°45′E to 62°E: Changes in plate-boundary geometry since 26 Ma, *Geochem. Geophys. Geosyst.*, *8*, Q06022, doi:10.1029/2006GC001559.

Batanova, V. G., G. Suhr, and A. V. Sobolev (1998), Origin of geochemical heterogeneity in the mantle peridotites from the Bay of Islands Ophiolite, Newfoundland, Canada: Ion probe study of clinopyroxenes, *Geochim. Cosmochim. Acta*, *62*(5), 853–866, doi:10.1016/S0016-7037(97)00384-0.

Blundy, J. D., T. J. Falloon, B. J. Wood, and J. A. Dalton (1995), Sodium partitioning between clinopyroxene and silicate melts, *J. Geophys. Res.*, *100*(B8), 15,501–15,515, doi:10.1029/95JB00954.

Bodinier, J. L., G. Vasseur, J. Vernieres, C. Dupuy, and J. Fabries (1990), Mechanisms of mantle metasomatism: Geochemical evidence from the Lherz orogenic peridotite, *J. Petrol.*, *31*(3), 597–628.

Bonatti, E., D. Brunelli, P. Fabretti, M. Ligi, R. A. Portaro, and M. Seyler (2001), Steady state creation of crust-free lithosphere at cold spots in mid-ocean ridges, *Geology*, *29*(11), 979–982, doi:10.1130/0091-7613(2001)029<0979:SSCOCF>2.0.CO;2.

Bottazzi, P., L. Ottolini, and R. Vannucci (1992), SIMS analyses of rare earth elements in natural minerals and glasses: An investigation of structural matrix effects on ion yields, *Scanning*, *14*, 160–168.

Bottinga, Y., and C. J. Allègre (1978), Partial melting under spreading ridges, *Philos. Trans. R. Soc. London A*, *288*, 501–525.

Brandon, A. D., J. E. Snow, R. J. Walker, J. W. Morgan, and T. D. Mock (2000), ^{190}Pt-^{186}Os and ^{187}Re-^{187}Os systematics of abyssal peridotites, *Earth Planet. Sci. Lett.*, *177*(3–4), 319–335, doi:10.1016/S0012-821X(00)00044-3.

Brey, G. P., and T. Köhler (1990), Geothermobarometry in four-phase Lherzolites II: New thermobarometers, and practical assessment of existing thermobarometers, *J. Petrol.*, *31*(6), 1353–1378.

Brunelli, D., and M. Seyler (2010), Asthenospheric percolation of alkaline melts beneath the St. Paul region (central Atlantic Ocean), *Earth Planet. Sci. Lett.*, *289*(3–4), 393–405, doi:10.1016/j.epsl.2009.11.028.

Brunelli, D., A. Cipriani, L. Ottolini, A. Peyve, and E. Bonatti (2003), Mantle peridotites from the Bouvet Triple Junction region, South Atlantic, *Terra Nova*, *15*(3), 194–203, doi:10.1046/j.1365-3121.2003.00482.x.

Brunelli, D., M. Seyler, A. Cipriani, L. Ottolini, and E. Bonatti (2006), Discontinuous melt extraction and weak refertilization of mantle peridotites at the Vema lithospheric section (Mid-Atlantic Ridge), *J. Petrol.*, *47*(4), 745–771, doi:10.1093/petrology/egi092.

Cannat, M., C. Rommevaux-Jestin, D. Sauter, C. Deplus, and V. Mendel (1999), Formation of the axial relief at the very slow spreading Southwest Indian Ridge (49° to 69°E), *J. Geophys. Res.*, *104*(B10), 22,825–22,843, doi:10.1029/1999JB900195.

Cannat, M., C. Rommevaux-Jestin, and H. Fujimoto (2003), Melt supply variations to a magma-poor ultraslow spreading ridge (Southwest Indian Ridge 61° to 69°E), *Geochem. Geophys. Geosyst.*, *4*(8), 9104, doi:10.1029/2002GC000480.

Cannat, M., D. Sauter, V. Mendel, E. Ruellan, K. Okino, J. Escartin, V. Combier, and M. Baala (2006), Modes of seafloor generation at a melt-poor ultraslow spreading ridge, *Geology*, *34*(7), 605–608, doi:10.1130/G22486.1.

Cannat, M., D. Sauter, A. Bezos, C. Meyzen, E. Humler, and M. Le Rigoleur (2008), Spreading rate, spreading obliquity, and melt supply at the ultraslow spreading Southwest Indian Ridge, *Geochem. Geophys. Geosyst.*, *9*, Q04002, doi:10.1029/2007GC001676.

Chu, D., and R. G. Gordon (1999), Evidence for motion between Nubia and Somalia along the Southwest Indian Ridge, *Nature*, *398*(6722), 64–67, doi:10.1038/18014.

Cipriani, A., H. K. Brueckner, E. Bonatti, and D. Brunelli (2004), Oceanic crust generated by elusive parents: Sr and Nd isotopes in basalt-peridotite pairs from the Mid-Atlantic Ridge, *Geology*, *32*(8), 657–660, doi:10.1130/G20560.1.

Dantas, C., G. Ceuleneer, M. Gregoire, M. Python, R. Freydier, J. Warren, and H. J. B. Dick (2007), Pyroxenites from the Southwest Indian Ridge, 9–16°E: Cumulates from incremental melt fractions produced at the top of a cold melting regime, *J. Petrol.*, *48*(4), 647–660, doi:10.1093/petrology/egl076.

DeMets, C., R. G. Gordon, D. F. Argus, and S. Stein (1990), Current plate motions, *Geophys. J. Int.*, *101*(2), 425–478, doi:10.1111/j.1365-246X.1990.tb06579.x.

Dick, H. J. B. (1989), Abyssal peridotites, very-slow spreading ridges and ocean ridge magmatism, in *Magmatism in the Ocean Basins*, edited by A. D. Saunders and M. J. Norry, *Geol. Soc. Spec. Publ.*, *42*, 71–105.

Dick, H. J. B., and T. B. Bullen (1984), Chromian spinel as a petrogenetic indicator in abyssal and alpine-type peridotites and spatially associated lavas, *Contrib. Mineral. Petrol.*, *86*, 54–76, doi:10.1007/BF00373711.

Dick, H. J. B., and R. L. Fisher (1984), Mineralogic studies of the residues of mantle melting: Abyssal and alpine-type peridotites, in *Kimberlites II: The Mantle and Crust-Mantle Relationships*, edited by J. Kornprobst, pp. 295–308, Elsevier, Amsterdam.

Dick, H. J. B., and J. H. Natland (1996), Late-stage melt evolution and transport in the shallow mantle beneath the East Pacific Rise, *Proc. Ocean Drill. Program Sci. Results*, *147*, 103–134.

Dick, H. J. B., R. L. Fisher, and W. B. Bryan (1984), Mineralogic variability of the uppermost mantle along mid-ocean ridges, *Earth Planet. Sci. Lett.*, *69*(1), 88–106, doi:10.1016/0012-821X(84)90076-1.

Dick, H. J. B., J. Lin, and H. Schouten (2003), An ultraslow spreading class of ocean ridge, *Nature*, *426*(6965), 405–412, doi:10.1038/nature02128.

Dijkstra, A. H., D. S. Sergeev, C. A. Spandler, T. Pettke, T. Meisel, and P. A. Cawood (2010), Highly refractory peridotites on Macquarie Island and the case for anciently depleted domains in the Earth's mantle, *J. Petrol.*, *51*, 469–493.

Downes, H., A. Beard, and R. Hinton (2004), Natural experimental charges: An ion-microprobe study of trace element distribution coefficients in glass-rich hornblendite and clinopyroxenite xenoliths, *Lithos*, *75*(1–2), 1–17, doi:10.1016/j.lithos.2003.12.013.

Fahey, A. J. (1998), Details of the measurement of rare earth and other trace element abundances by secondary ion mass spectrometry, *Int. J. Mass Spectrom.*, *176*(1–2), 63–76, doi:10.1016/S1387-3806(98)14006-X.

Godard, M., D. Jousselin, and J.-L. Bodinier (2000), Relationships between geochemistry and structure beneath a palaeo spreading centre: A study of the mantle section in the Oman ophiolite, *Earth Planet. Sci. Lett.*, *180*(1–2), 133–148, doi:10.1016/S0012-821X(00)00149-7.

Godard, M., Y. Lagabrielle, O. Alard, and J. Harvey (2008), Geochemistry of the highly depleted peridotites drilled at ODP Sites 1272 and 1274 (Fifteen-Twenty Fracture Zone, Mid-Atlantic Ridge): Implications for mantle dynamics beneath a slow spreading ridge, *Earth Planet. Sci. Lett.*, *267*(3–4), 410–425, doi:10.1016/j.epsl.2007.11.058.

Green, D. H., and A. E. Ringwood (1967), The genesis of basaltic magmas, *Contrib. Mineral. Petrol.*, *15*, 103–190, doi:10.1007/BF00372052.

Green, D. H., W. O. Hibberson, and A. L. Jaques (1979), Petrogenesis of mid-ocean ridge basalts, in *The Earth: Its Origin, Structure and Evolution*, edited by M. W. McElthinney, pp. 265–299, Academic, San Diego, Calif.

Günther, D., and C. A. Heinrich (1999), Enhanced sensitivity in laser ablation-ICP mass spectrometry using helium-argon mixtures as aerosol carrier, *J. Anal. At. Spectrom.*, *14*(9), 1363–1368, doi:10.1039/a901648a.

Harvey, J., A. Gannoun, K. W. Burton, N. W. Rogers, O. Alard, and I. J. Parkinson (2006), Ancient melt extraction from the oceanic upper mantle revealed by Re-Os isotopes in abyssal peridotites from the Mid-Atlantic Ridge, *Earth Planet. Sci. Lett.*, *244*(3–4), 606–621, doi:10.1016/j.epsl.2006.02.031.

Hellebrand, E., and J. E. Snow (2003), Deep melting and sodic metasomatism underneath the highly oblique spreading Lena Trough (Arctic Ocean), *Earth Planet. Sci. Lett.*, *216*(3), 283–299, doi:10.1016/S0012-821X(03)00508-9.

Hellebrand, E., J. E. Snow, H. J. B. Dick, and A. W. Hofmann (2001), Coupled major and trace elements as indicators of the extent of melting in mid-ocean ridge peridotites, *Nature*, *410*(6829), 677–681, doi:10.1038/35070546.

Hellebrand, E., J. E. Snow, P. Hoppe, and A. W. Hofmann (2002a), Garnet field melting and late-stage refertilization in 'residual' abyssal peridotites from the Central Indian Ridge, *J. Petrol.*, *43*(12), 2305–2338, doi:10.1093/petrology/43.12.2305.

Hellebrand, E., J. E. Snow, and R. Mühe (2002b), Mantle melting beneath Gakkel Ridge (Arctic Ocean): Abyssal peridotite spinel compositions, *Chem. Geol.*, *182*(2–4), 227–235, doi:10.1016/S0009-2541(01)00291-1.

Hellebrand, E., J. Snow, S. Mostefaoui, and P. Hoppe (2005), Trace element distribution between orthopyroxene and clinopyroxene in peridotites from the Gakkel Ridge: A SIMS and NanoSIMS study, *Contrib. Mineral. Petrol.*, *150*(5), 486–504.

Horner-Johnson, B. C., R. G. Gordon, S. M. Cowles, and D. F. Argus (2005), The angular velocity of Nubia relative to Somalia and the location of the Nubia–Somalia–Antarctica triple junction, *Geophys. J. Int.*, *162*(1), 221–238, doi:10.1111/j.1365-246X.2005.02608.x.

Irving, A. J., and F. A. Frey (1984), Trace element abundances in megacrysts and their host basalts: Constraints on partition coefficients and megacryst genesis, *Geochim. Cosmochim. Acta*, *48*(6), 1201–1221, doi:10.1016/0016-7037(84)90056-5.

Jaques, A. L., and D. H. Green (1980), Anhydrous melting of peridotite at 0–15 Kb pressure and the genesis of tholeiitic basalts, *Contrib. Mineral. Petrol.*, *73*(3), 287–310.

Johnson, K. T. M., and H. J. B. Dick (1992), Open system melting and temporal and spatial variation of peridotite and basalt at the Atlantis II Fracture Zone, *J. Geophys. Res.*, *97*(B6), 9219–9241, doi:10.1029/92JB00701.

Johnson, K. T. M., H. J. B. Dick, and N. Shimizu (1990), Melting in the oceanic upper mantle: An ion microprobe study of diopsides in abyssal peridotites, *J. Geophys. Res.*, *95*(B3), 2661–2678, doi:10.1029/JB095iB03p02661.

Jokat, W., O. Ritzmann, M. C. Schmidt-Aursch, S. Drachev, S. Gauger, and J. Snow (2003), Geophysical evidence for reduced melt production on the Arctic ultraslow Gakkel mid-ocean ridge, *Nature*, *423*(6943), 962–965, doi:10.1038/nature01706.

Juteau, T., E. Berger, and M. Cannat (1990), Serpentinized, residual mantle peridotites from the M. A. R. median valley, ODP Hole 670A (21°10′N, 45°02′W, Leg 109), Primary mineralogy and geothermometry, *Proc. Ocean Drill. Program Sci. Results*, *106/109*, 27–45.

Kelemen, P. B., H. J. B. Dick, and J. E. Quick (1992), Formation of harzburgite by pervasive melt/rock reaction in the upper mantle, *Nature*, *358*(6388), 635–641, doi:10.1038/358635a0.

Kelemen, P. B., J. A. Whitehead, E. Aharonov, and K. A. Jordahl (1995), Experiments on flow focusing in soluble porous media, with applications to melt extraction from the mantle, *J. Geophys. Res.*, *100*(B1), 475–496, doi:10.1029/94JB02544.

Kelemen, P. B., G. M. Yogodzinski, and D. W. Scholl (2004), Alongstrike variation in lavas of the Aleutian island arc: Implications for the genesis of high Mg# andesite and the continental crust, in *Inside the Subduction Factory*, *Geophys. Monogr. Ser.*, vol. 138, edited by J. Eiler, pp. 223–276, AGU, Washington, D. C.

Kelemen, P. B., E. Kikawa, D. J. Miller, and the Scientific Shipboard Party (2007), Leg 209 summary: Processes in a 20-km-thick conductive boundary layer beneath the Mid-Atlantic Ridge, 14°–16°N, *Proc. Ocean Drill. Program Sci. Results*, *209*, 1–33.

Klein, E. M., and C. H. Langmuir (1987), Global correlations of ocean ridge basalt chemistry with axial depth and crustal thickness, *J. Geophys. Res.*, *92*(B8), 8089–8115, doi:10.1029/JB092iB08p08089.

Kogiso, T., M. M. Hirschmann, and P. W. Reiners (2004), Length scales of mantle heterogeneities and their relationship to ocean island basalt geochemistry, *Geochim. Cosmochim. Acta*, *68*(2), 345–360, doi:10.1016/S0016-7037(03)00419-8.

Langmuir, C. H., E. M. Klein, and T. Plank (1992), Petrological systematics of mid-ocean ridge basalts: Constraints on melt generation beneath ocean ridges, in *Mantle Flow and Melt Generation at Mid-Ocean Ridges*, *Geophys. Monogr. Ser.*, vol. 71, edited by J. Phipps Morgan, D. K. Blackman, and J. M. Sinton, pp. 183–280, AGU, Washington, D.C.

Le Roex, A. P., H. J. B. Dick, A. J. Erlank, A. M. Reid, F. A. Frey, and S. R. Hart (1983), Geochemistry, mineralogy and petrogenesis of lavas erupted along the Southwest Indian

Ridge between the Bouvet Triple Junction and 11 degrees east, *J. Petrol.*, *24*(3), 267–318.

Le Roex, A. P., H. J. B. Dick, and R. T. Watkins (1992), Petrogenesis of anomalous K-enriched MORB from the Southwest Indian Ridge: 11°53′E to 14°38′E, *Contrib. Mineral. Petrol.*, *110*(2–3), 253–268, doi:10.1007/BF00310742.

Lee, K. L. (1997), Petrological and geochemical studies of an abyssal peridotite from the Atlantis II Fracture Zone, M.S. thesis, MIT/WHOI Joint Program, Woods Hole, Mass.

Lee, C.-T. A., A. Harbert, and W. P. Leeman (2007), Extension of lattice strain theory to mineral/mineral rare-earth element partitioning: An approach for assessing disequilibrium and developing internally consistent partition coefficients between olivine, orthopyroxene, clinopyroxene and basaltic melt, *Geochim. Cosmochim. Acta*, *71*(2), 481–496, doi:10.1016/j.gca.2006.09.014.

Lemaux, J., II, R. G. Gordon, and J.-Y. Royer (2002), Location of the Nubia-Somalia boundary along the Southwest Indian Ridge, *Geology*, *30*(4), 339–342, doi:10.1130/0091-7613(2002)030<0339:LOTNSB>2.0.CO;2.

Liang, Y. (2008), Simple models for dynamic melting in an upwelling heterogeneous mantle column: Analytical solutions, *Geochim. Cosmochim. Acta*, *72*(15), 3804–3821, doi:10.1016/j.gca.2008.05.050.

Liang, Y., and Q. Peng (2010), Non-modal melting in an upwelling mantle column: Steady-state models with applications to REE depletion in abyssal peridotites and the dynamics of melt migration in the mantle, *Geochim. Cosmochim. Acta*, *74*(1), 321–339, doi:10.1016/j.gca.2009.09.029.

Liu, C. Z., J. E. Snow, E. Hellebrand, G. Brugmann, A. von der Handt, A. Buchl, and A. W. Hofmann (2008), Ancient, highly heterogeneous mantle beneath Gakkel ridge, Arctic Ocean, *Nature*, *452*(7185), 311–316, doi:10.1038/nature06688.

Lundstrom, C. C. (2000), Rapid diffusive infiltration of sodium into partially molten peridotite, *Nature*, *403*(6769), 527–530, doi:10.1038/35000546.

Mazzucchelli, M., G. Rivalenti, D. Brunelli, A. Zanetti, and E. Boari (2009), Formation of highly refractory dunite by focused percolation of pyroxenite-derived melt in the Balmuccia peridotite massif (Italy), *J. Petrol.*, *50*(7), 1205–1233, doi:10.1093/petrology/egn053.

McKenzie, D., and M. J. Bickle (1988), The volume and composition of melt generated by extension of the lithosphere, *J. Petrol.*, *29*, 625–679.

Mendel, V., D. Sauter, L. Parson, and J.-R. Vanney (1997), Segmentation and morphotectonic variations along a super slow spreading center: The Southwest Indian Ridge (57°E–70°E), *Mar. Geophys. Res.*, *19*(6), 505–533, doi:10.1023/A:1004232506333.

Mével, C., P. Agrinier, M. Cannat, and the EDUL Cruise Scientific Party (1997), Sampling the Southwest Indian Ridge: First results of the EDUL cruise (R/V *Marion Dufresne II*, August 1997), *InterRidge News*, *6*(2), 25–26.

Meyzen, C. M., M. J. Toplis, E. Humler, J. N. Ludden, and C. Mevel (2003), A discontinuity in mantle composition beneath the Southwest Indian Ridge, *Nature*, *421*(6924), 731–733, doi:10.1038/nature01424.

Meyzen, C. M., J. N. Ludden, E. Humler, B. Luais, M. J. Toplis, C. Mével, and M. Storey (2005), New insights into the origin and distribution of the DUPAL isotope anomaly in the Indian Ocean mantle from MORB of the Southwest Indian Ridge, *Geochem. Geophys. Geosyst.*, *6*, Q11K11, doi:10.1029/2005GC000979.

Michael, P. J., et al. (2003), Magmatic and amagmatic seafloor generation at the ultraslow spreading Gakkel ridge, Arctic Ocean, *Nature*, *423*(6943), 956–961, doi:10.1038/nature01704.

Minshull, T. A., M. R. Muller, and R. S. White (2006), Crustal structure of the Southwest Indian Ridge at 66°E: Seismic constraints, *Geophys. J. Int.*, *166*(1), 135–147, doi:10.1111/j.1365-246X.2006.03001.x.

Morishita, T., K. Hara, K. Nakamura, T. Sawaguchi, A. Tamura, S. Arai, K. Okino, K. Takai, and H. Kumagai (2009), Igneous, alteration and exhumation processes recorded in abyssal peridotites and related fault rocks from an oceanic core complex along the Central Indian Ridge, *J. Petrol.*, *50*(7), 1299–1325, doi:10.1093/petrology/egp025.

Muller, M. R., C. J. Robinson, T. A. Minshull, R. S. White, and M. J. Bickle (1997), Thin crust beneath ocean drilling program borehole 735B at the Southwest Indian Ridge?, *Earth Planet. Sci. Lett.*, *148*(1–2), 93–107, doi:10.1016/S0012-821X(97)00030-7.

Muller, M. R., T. A. Minshull, and R. S. White (1999), Segmentation and melt supply at the Southwest Indian Ridge, *Geology*, *27*(10), 867–870, doi:10.1130/0091-7613(1999)027<0867:SAMSAT>2.3.CO;2.

Navon, O., and E. M. Stolper (1987), Geochemical consequences of melt percolation: The upper mantle as a chromatographic column, *J. Geol.*, *95*(3), 285–307, doi:10.1086/629131.

Ozawa, K., and N. Shimizu (1995), Open-system melting in the upper mantle: Constraints from the Hayachine-Miyamori ophiolite, northeastern Japan, *J. Geophys. Res.*, *100*(B11), 22,315–22,335, doi:10.1029/95JB01967.

Parkinson, I. J., J. A. Pearce, M. F. Thirlwall, K. T. M. Johnson, and G. Ingram (1992), Trace element geochemistry of peridotites from the Izu-Bonin, Mariana forearc, Leg 125, *Proc. Ocean Drill. Program Sci. Results*, *125*, 487–506.

Patriat, P., and J. Segoufin (1988), Reconstruction of the Central Indian Ocean, *Tectonophysics*, *155*(1–4), 211–234, doi:10.1016/0040-1951(88)90267-3.

Patriat, P., D. Sauter, M. Munschy, and L. Parson (1997), A survey of the Southwest Indian Ridge axis between Atlantis II Fracture Zone and the Indian Ocean Triple Junction: Regional setting and large scale segmentation, *Mar. Geophys. Res.*, *19*(6), 457–480, doi:10.1023/A:1004312623534.

Pearce, N. J. G., W. T. Perkins, J. A. Westgate, M. P. Gorton, S. E. Jackson, C. R. Neal, and S. P. Chenery (1997), A compilation of new and published major and trace element data for NIST SRM 610 and NIST SRM 612 glass reference materials, *Geostand. Newsl.*, *21*(1), 115–144, doi:10.1111/j.1751-908X.1997.tb00538.x.

Phipps Morgan, J., and E. M. Parmentier (1995), Crenulated seafloor: Evidence for spreading-rate dependent structure of mantle upwelling and melting beneath a mid-oceanic spreading center, *Earth Planet. Sci. Lett.*, *129*(1–4), 73–84, doi:10.1016/0012-821X(94)00227-P.

Plá Cid, J., L. V. Stoll Nardi, P. E. Gisbert, C. Merlet, and B. Boyer (2005), SIMS analyses on trace and rare earth elements in coexisting clinopyroxenes and micas from minette mafic enclaves in potassic syenites crystallized under high pressures, *Contrib. Mineral. Petrol.*, *148*(6), 675–688, doi:10.1007/s00410-004-0626-7.

Rabinowicz, M., and M. J. Toplis (2009), Melt segregation in the lower part of the partially molten mantle zone beneath an oceanic spreading centre: Numerical modelling of the combined effects of shear segregation and compaction, *J. Petrol.*, *50*(6), 1071–1106, doi:10.1093/petrology/egp033.

Rampone, E., A. W. Hofmann, G. B. Piccazrdo, R. Vannucci, P. Bottazzi, and L. Ottolini (1996), Trace element and isotope geochemistry of depleted peridotites from an N-MORB type ophiolite (Internal Liguride, *N. Italy), Contrib. Mineral. Petrol.*, *123*, 61–76, doi:10.1007/s004100050143.

Rocholl, A. B. E., et al. (1997), Chemical characterisation of NIST silicate glass certified reference material SRM 610 by ICP-MS, TIMS, LIMS, SSMS, INAA, AAS and PIXE, *Geostand. Newsl.*, *21*(1), 101–114, doi:10.1111/j.1751-908X.1997.tb00537.x.

Rommevaux-Jestin, C., C. Deplus, and P. Patriat (1997), Mantle Bouguer Anomaly along an ultra slow spreading ridge: Implications for accretionary processes and comparison with results from central Mid-Atlantic Ridge, *Mar. Geophys. Res.*, *19*(6), 481–503, doi:10.1023/A:1004269003009.

Ross, K., and D. Elthon (1997), Extreme incompatible trace-element depletion of diopside in residual mantle from south of Kane F.Z, *Proc. Ocean Drill. Program Sci. Results*, *157*, 277–284.

Salters, V. J. M., and H. J. B. Dick (2002), Mineralogy of the mid-ocean-ridge basalt source from neodymium isotopic composition of abyssal peridotites, *Nature*, *418*(6893), 68–72, doi:10.1038/nature00798.

Sandwell, D. T., and W. H. F. Smith (1997), Marine gravity anomaly from Geosat and ERS 1 satellite altimetry, *J. Geophys. Res.*, *102*(B5), 10,039–10,054, doi:10.1029/96JB03223.

Sauter, D., P. Patriat, C. Rommevaux-Jestin, M. Cannat, and A. Briais (2001), The Southwest Indian Ridge between 49°15′E and 57°E: Focused accretion and magma redistribution, *Earth Planet. Sci. Lett.*, *192*(3), 303–317, doi:10.1016/S0012-821X(01)00455-1.

Seyler, M., M. J. Toplis, J.-P. Lorand, A. Luguet, and M. Cannat (2001), Clinopyroxene microtextures reveal incompletely extracted melts in abyssal peridotites, *Geology*, *29*(2), 155–158, doi:10.1130/0091-7613(2001)029<0155:CMRIEM>2.0.CO;2.

Seyler, M., M. Cannat, and C. Mével (2003), Evidence for major-element heterogeneity in the mantle source of abyssal peridotites from the Southwest Indian Ridge (52° to 68°E), *Geochem. Geophys. Geosyst.*, *4*(2), 9101, doi:10.1029/2002GC000305.

Seyler, M., J.-P. Lorand, M. J. Toplis, and G. Godard (2004), Asthenospheric metasomatism beneath the mid-ocean ridge: Evidence from depleted abyssal peridotites, *Geology*, *32*(4), 301–304, doi:10.1130/G20191.1.

Seyler, M., J. Lorand, H. Dick, and M. Drouin (2007), Pervasive melt percolation reactions in ultra-depleted refractory harzburgites at the Mid-Atlantic Ridge, 15°20′N: ODP Hole 1274A, *Contrib. Mineral. Petrol.*, *153*(3), 303–319, doi:10.1007/s00410-006-0148-6.

Shannon, R. (1976), Revised effective ionic radii and systematic studies of interatomic distances in halides and chalcogenides, *Acta Crystallogr., Sect. A Cryst. Phys. Diffr. Theor. Gen. Crystallogr.*, *32*(5), 751–767, doi:10.1107/S0567739476001551.

Shaw, D. M. (2000), Continuous (dynamic) melting theory revisited, *Can. Mineral.*, *38*(5), 1041–1063, doi:10.2113/gscanmin.38.5.1041.

Shimizu, N., M. P. Semet, and C. J. Allègre (1978), Geochemical applications of quantitative ion-microprobe analysis, *Geochim. Cosmochim. Acta*, *42*(9), 1321–1334, doi:10.1016/0016-7037(78)90037-6.

Smith, W. H. F., and D. T. Sandwell (1994), Bathymetric prediction from dense satellite altimetry and sparse shipboard bathymetry, *J. Geophys. Res.*, *99*(B11), 21,803–21,824, doi:10.1029/94JB00988.

Snow, J. E., S. R. Hart, and H. J. B. Dick (1994), Nd and Sr isotope evidence linking mid-ocean-ridge basalts and abyssal peridotites, *Nature*, *371*(6492), 57–60, doi:10.1038/371057a0.

Spiegelman, M., and P. B. Kelemen (2003), Extreme chemical variability as a consequence of channelized melt transport, *Geochem. Geophys. Geosyst.*, *4*(7), 1055, doi:10.1029/2002GC000336.

Standish, J. J., H. J. B. Dick, P. J. Michael, W. G. Melson, and T. O'Hearn (2008), MORB generation beneath the ultra-slow spreading Southwest Indian Ridge (9°–25°E): Major element chemistry and the importance of process versus source, *Geochem. Geophys. Geosyst.*, *9*, Q05004, doi:10.1029/2008GC001959.

Stracke, A., and B. Bourdon (2009), The importance of melt extraction for tracing mantle heterogeneity, *Geochim. Cosmochim. Acta*, *73*(1), 218–238, doi:10.1016/j.gca.2008.10.015.

Takazawa, E., F. A. Frey, N. Shimizu, M. Obata, and J. L. Bodinier (1992), Geochemical evidence for melt migration and reaction in the upper mantle, *Nature*, *359*(6390), 55–58, doi:10.1038/359055a0.

Van Achterberg, E., C. G. Ryan, S. E. Jackson, and W. Griffin (2001), Data reduction software for LA-ICP-MS, in *Laser Ablation ICP-MS in the Earth Science*, edited by P. Sylvester, *Short Course Ser. Mineral. Assoc. Can.*, *40*, 239–243.

Warren, J. M., and N. Shimizu (2010), Cryptic variations in abyssal peridotite compositions: Evidence for shallow-level melt infiltration in the oceanic lithosphere, *J. Petrol.*, *51*(1–2), 395–423, doi:10.1093/petrology/egp096.

Warren, J. M., N. Shimizu, C. Sakaguchi, H. J. B. Dick, and E. Nakamura (2009), An assessment of upper mantle heterogeneity based on abyssal peridotite isotopic compositions, *J. Geophys. Res.*, *114*, B12203, doi:10.1029/2008JB006186.

Witt-Eickschen, G., and H. S. C. O'Neill (2005), The effect of temperature on the equilibrium distribution of trace elements between clinopyroxene, orthopyroxene, olivine and spinel in upper mantle peridotite, *Chem. Geol.*, *221*(1–2), 65–101, doi:10.1016/j.chemgeo.2005.04.005.

Zinner, E., and G. Crozaz (1986), A method for the quantitative measurement of rare earth elements in the ion microprobe, *Int. J. Mass Spectrom. Ion Processes*, *69*(1), 17–38, doi:10.1016/0168-1176(86)87039-2.

Zou, H. (1998), Trace element fractionation during modal and nonmodal dynamic melting and open-system melting: A mathematical treatment, *Geochim. Cosmochim. Acta*, *62*(11), 1937–1945, doi:10.1016/S0016-7037(98)00115-X.